

---

# Computer Simulations of Planetary Rings (29.1.2016)

H. SALO, K. OHTSUKI AND M. C. LEWIS

The local dynamics of planetary rings is governed by the orbital motion, the frequent impacts between ring particles, their mutual self-gravity, and the perturbations exerted by external satellites and embedded moonlets. In Saturn's dense A and B rings the particles collide  $\sim 100$  times per orbital revolution. Although the orbital velocities are  $\sim 20$  km/s, the random velocities related to orbital eccentricities and inclinations are small, of the order of few mm/s (this corresponds to a ring vertical thickness of few tens of meters, excluding strongly perturbed regions). Such gentle impacts do not lead to fragmentation, but still dissipate a significant fraction of random kinetic energy in each collision. This loss is balanced by the viscous gain of energy from the orbital motion around the planet, resulting in a local steady-state in a time scale of few tens of impacts/particle (Hämeen-Anttila, 1978; Goldreich and Tremaine, 1978; Stewart et al., 1984). Characteristics of this energy balance (such as velocity dispersion, geometric thickness, and viscosity) are determined by the frequency and elasticity of impacts, and by the internal density and size distribution of particles. In much longer timescales the ring radial evolution is governed by viscous evolution. Depending on the viscosity-density relation following from the energy balance, the ring can be either stable or unstable against the viscous growth of local perturbations. For example, dense rings composed of quite inelastic particles can become viscously overstable, while less dissipative particle may be prone to viscous instability.

The fundamental importance of ring particles' feeble mutual gravity for shaping the fine structure of Saturn's rings is strikingly demonstrated by the Cassini stellar (Colwell et al., 2006, 2007; Hedman et al., 2007) and radio occultation measurements (Thomson et al., 2007), which confirm the presence of unresolved trailing structures (self-gravity wakes (Salo, 1992a)) throughout the A and B rings. These transient, continuously regenerated trailing density enhancements arise as a superposition of tiny wakes excited around each individual ring particle, amplified by the interplay of shear and gravity (swing-amplification mechanism (Toomre, 1981; Goldreich and Lynden-Bell, 1965)). Such structures were envisioned by Alar Toomre already decades ago (Julian and Toomre, 1966), though in a very different context (and scale - kpcs rather than tens of meters), as a suggestion of how to create and maintain spiral structure in galactic stellar disks. In planetary rings the dissipative impacts between particles provide a natural mechanism which keeps the rings dynamically cool and reactive to such gravitational disturbances. For the same reason the excitation of spiral den-

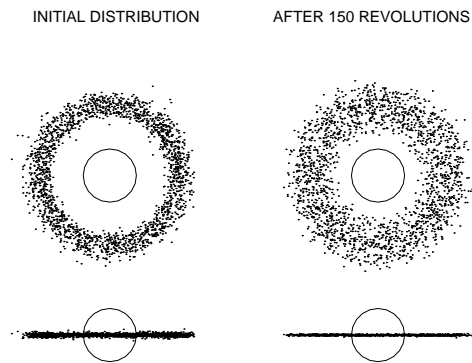


**Figure 1.1** Simulation example of azimuthally complete ring. The number of particles  $N=2000$ , and the particle radius is  $0.005a$ , where  $a$  is the mean distance of particles. The initial width of the ring is  $0.2a$ , yielding an optical depth  $\tau = 0.125$ . The impacts are described with a constant coefficient of restitution  $\epsilon_n = 0.5$ . During 150 orbital revolution each particle have experienced on the average about 250 impacts: the system has flattened to a few particle diameter thick disk, and has at the same time nearly doubled its radial width.

sity waves at satellite resonance locations (?) - another concept originally developed in the context of galaxy dynamics - has its clearest manifestation in Saturn's rings (Burns and Cuzzi, 2006; Cuzzi et al., 2010); Saturn's rings also provide the most extreme examples of disk warping (Hedman et al., 2011), and the perturbing effect of embedded mass concentrations on the surrounding particles ('propellers') (Cuzzi et al., 2010).

This Chapter reviews numerical N-body simulations of self-gravitating, mutually colliding particles, concentrating on a local method, where the evolution of a small ring patch co-moving with the mean orbital motion is followed. After reviewing the main ingredients of the simulations in Sect. 1.2 (dynamical equations, treatment of boundaries, impacts, and self-gravity), we illustrate the basic mechanisms affecting the local energy balance (Sect. 1.8), and give simulation examples of self-gravity wakes (Sect. 1.8.2) and non-linear structures resulting from viscous overstability and instability (Sect. 1.9). For detailed theoretical background, see Chapters XX. For simulations including external perturbations and dealing with the large scale evolution of the rings, see Chapters YY.

### 1.1 Early simulation studies

The pioneering simulation studies of the collisional evolution of planetary rings were performed in the 1970s, by Trulsen (1972), Brahic (1977) and Hämeen-Anttila and Lukkari (1980). All these simulations used the same basic approach: a complete ring of particles revolving the central body in Keplerian orbits. The particles were identical hard spheres, and impacts were treated as leading to instantaneous changes of relative velocity vectors. Since only a few hundred particles could be followed with the available computer capacity, these simulations were limited to low optical depth  $\tau \lesssim 10^{-3}$ . The particle sizes were unrealistically large compared to the width of the ring, which made it difficult, for example, to separate the time scales for the establishment of local steady-state velocity dispersion from the viscous radial spreading (see Fig. 1.1). Nevertheless, many basic characteristics of collisional systems (see Section 1.8) were discovered, including the existence of a critical upper limit for the coefficient of restitution  $\varepsilon_{cr}$ , required for a stable thermal balance in the case of constant  $\varepsilon_n$  (Trulsen, 1972), a minimum residual velocity dispersion of the order of few times  $R\Omega$  (Brahic, 1977), where  $\Omega$  is the local angular velocity and  $R$  the particle radius, and the establishment of equilibrium with a finite velocity dispersion in a case of a velocity-dependent coefficient of restitution (Hämeen-Anttila and Lukkari, 1980). These simulations also served as important checks for various analytical treatments (see Stewart et al. (1984)). Brahic (1977) also provided the first constraints for the velocity dispersion in Saturn's rings, in terms of timescales for viscous spreading. However, a fundamental breakthrough was provided by the Wisdom and Tremaine (1988) application of local method to planetary ring simulations.

In contrast to the simulations of a complete ring, in local simulations all calculations are restricted to a small region co-moving with the mean orbital motion of the particles (Fig. 1.2). This allows to extend the simulations to high optical depths, with realistic particle sizes. However, due to systematic velocity shear individual particles will rapidly leave the calculation region. As described in detail below, this is taken into account by periodic boundary conditions, returning the leaving particles to the calculation region with properly modified position and velocity vectors. An important advantage of the method is that it facilitates the study of local steady-state properties as a function of fixed optical depth. The larger-scale viscous evolution can then be deduced from the viscosity-density relation derived from a set of small-scale simulations for different optical depths. This is justified, based on the large separation of time scales for the establishment of the local thermal balance ( $\propto (\tau\Omega)^{-1}$ ), and the much longer time scales for the radial evolution ( $\propto W^2/\nu \propto (\tau\Omega)^{-1}(W/H)^2$ , where  $\nu$  is the kinematic viscosity,  $W$  is the radial scale of interest, and  $H$  is the ring vertical thickness).

The local method, developed for Molecular Dynamics simulations by Lees and Edwards (1972), was first applied to planetary rings by Wisdom and Tremaine (1988) and to stellar disks by Toomre and Kalnajs (1991). In the former study

impacts between identical particles were taken into account, but not their mutual gravity, whereas the latter study concentrated only on gravitational forces. In Salo (1992a) both, gravity and impacts, were simultaneously included. Since then, the local method has been extensively used (Richardson, 1993, 1994; Daisaka and Ida, 1999; Daisaka et al., 2001; Ohtsuki, 1999, e.g.).

### 1.2 The Local Simulation Method

The coordinate system in the local method has its origin at  $\vec{r}_0$ , a reference point orbiting the planet of mass  $M$  in a circular orbit at the distance  $a$ , with a constant angular velocity  $\Omega = \sqrt{GM/a^3}$ . The x-axis points in the radial direction, the y-axis in the direction of orbital motion, and the z-axis is perpendicular to the equatorial plane, parallel to the angular velocity vector  $\vec{\Omega} = \Omega\hat{z}$ . Since a rotating reference frame is used, the equations of motion are

$$\ddot{\vec{r}} + 2\vec{\Omega} \times \dot{\vec{r}} + \vec{\Omega} \times (\vec{\Omega} \times \vec{r}) = \vec{F}_c/m + \vec{F}/m \quad (1.1)$$

where  $\vec{r} = (x, y, z)$  is a particle's radius vector with respect to  $\vec{r}_0$ ,  $\vec{F}_c$  denotes the central force of the particle relative to the force at  $\vec{r}_0$ ,  $\vec{F}$  the additional forces, and the two last terms on the left hand side represent the Coriolis and centrifugal terms, respectively. For the Keplerian case (spherically symmetric central body) the difference in the acceleration due to central field is

$$\begin{aligned} \vec{F}_c/m &= -GM \left( \frac{\vec{r}_0 + \vec{r}}{|\vec{r}_0 + \vec{r}|^3} - \frac{\vec{r}_0}{a^3} \right) \\ &\approx -\frac{GM}{a^3} \left( \vec{r} - 3\frac{\vec{r} \cdot \vec{r}_0}{a^2} \vec{r}_0 \right) \\ &= \Omega^2(2x, -y, -z), \end{aligned} \quad (1.2)$$

if only terms linear in  $|\vec{r}|/a$  are retained. In the more general case where the azimuthal, radial, and vertical frequencies ( $\Omega$ ,  $\kappa$ , and  $\Omega_z$ ) are different from each other,

$$\vec{F}_c/m = \left( (3\Omega^2 - \kappa^2)x, -\Omega^2y, -\Omega_z^2z \right), \quad (1.3)$$

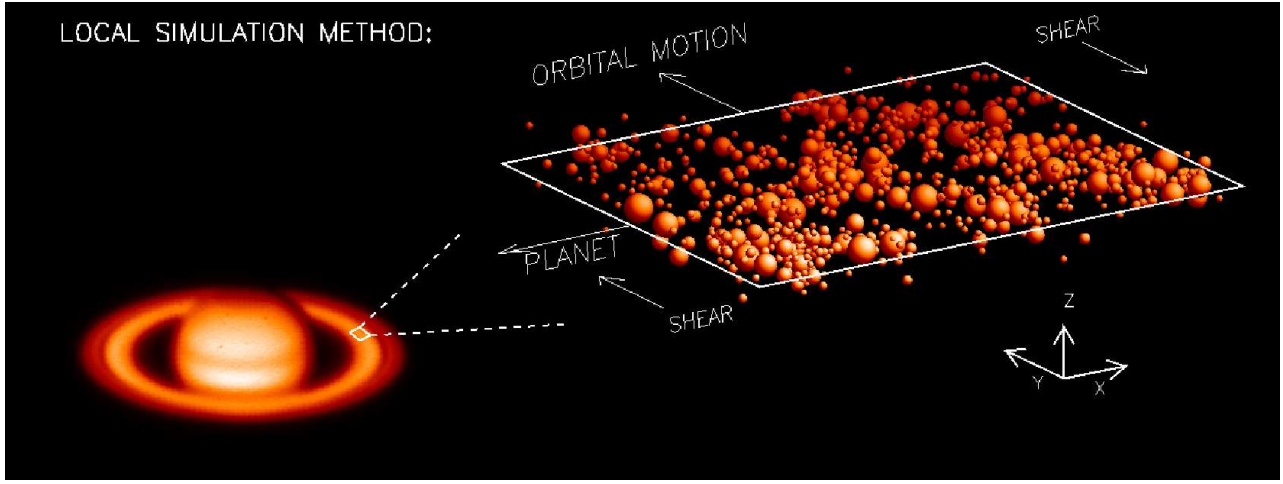
with

$$\begin{aligned} \Omega^2 &= \frac{F_r}{r} \Big|_{\vec{r}=\vec{r}_o}, \\ \kappa^2 &= \frac{1}{r^3} \frac{d}{dr} (r^3 F_r) \Big|_{\vec{r}=\vec{r}_o}, \\ \Omega_z^2 &= \frac{d}{dz} (F_z) \Big|_{\vec{r}=\vec{r}_o}, \end{aligned}$$

where  $F_r$  and  $F_z$  are the radial and vertical components of the central force. Inserting this to Eq. (1.1) yields

$$\begin{aligned} \ddot{x} - 2\Omega\dot{y} + (\kappa^2 - 4\Omega^2)x &= F_x/m, \\ \ddot{y} + 2\Omega\dot{x} &= F_y/m, \\ \ddot{z} + \Omega_z^2 z &= F_z/m, \end{aligned} \quad (1.4)$$

where  $F_x, F_y, F_z$  denote additional forces besides the central force, e.g. due to impacts and particles' mutual gravity. This is the familiar Hill-approximation, describing the elliptical motion in terms of epicycles superposed on the circular



motion of the guiding centre. In the absence of additional forces Eqs. (1.4) have the solution

$$\begin{aligned} x &= x_0 - A \cos[\kappa(t - t_0)], \\ y &= y_0 + \frac{2\Omega A}{\kappa} \sin[\kappa(t - t_0)] + \frac{\kappa^2 - 4\Omega^2}{2\Omega} x_0 t, \\ z &= B \sin[\Omega_z(t - t_1)], \end{aligned} \quad (1.5)$$

where  $x_0, y_0, A, t_0, B, t_1$  are six constants of integration:  $x_0$  and  $y_0$  are given by the guiding centre location at  $t = 0$ , while  $A = ea, B = ia$  correspond to eccentricity and inclination, and  $t_0, t_1$  to the times of pericenter and ascending node passage, respectively. The guiding centre drifts tangentially with the speed  $sx_0$ , where the shear rate

$$s = \frac{\kappa^2 - 4\Omega^2}{2\Omega} \quad (1.6)$$

reduces to  $s = -\frac{3}{2}\Omega$  in the Keplerian case.

The use of linearized equations is physically well justified, as the typical particle excursion from circular orbit may be expected to be at least a factor of  $10^{-6}$  smaller than  $a$ . Furthermore, through the linearization the set of Eqs. (1.4) is invariant under the transformation

$$\begin{aligned} (x', y', z') &= (x + \Delta x, y + \Delta y + \Delta x st, z) \\ (v'_x, v'_y, v'_z) &= (v_x, v_y + \Delta x s, v_z), \end{aligned} \quad (1.7)$$

where  $\Delta x$  and  $\Delta y$  denote arbitrary shifts in radial and tangential directions, respectively. This allows to use simple periodic boundary conditions for simulations: using  $\Delta x = n_x L_x$  and  $\Delta y = n_y L_y$ , where  $n_x$  and  $n_y$  are integers, and  $L_x$  and  $L_y$  denote the radial and tangential dimensions of the calculation region,

$$\begin{aligned} (x', y', z') &= (x + n_x L_x, y + n_y L_y + n_x L_x st, z), \\ (v'_x, v'_y, v'_z) &= (v_x, v_y + n_x L_x s, v_z), \end{aligned} \quad (1.8)$$

with  $|n_x|, |n_y| = 1, 2, \dots$ , define a set of image particles (replicas, see Fig. 1.3), so that each particle leaving the actual calculation region ( $|x| > L_x/2$  or  $|y| > L_y/2$ ), is replaced by one of its replicas which enters the region from the opposite face, with appropriately modified position and velocity. Especially, if the particle crosses the outer or inner radial boundary, the tangential velocity of the particle is modified by  $\Delta v_y = \pm s L_x$ , which corresponds to the difference

**Figure 1.2** Schematic representation of the local simulation method (“shearing brick” method) (see text for explanation).

of shear velocity across  $L_x$ . Since the mean tangential velocity at the radial coordinate  $x$  equals  $sx$ , this leaves the shear corrected tangential velocity  $v_y - sx$  unaffected. With the use of these periodic boundary conditions the evolution of the system is independent of the choice of the origin of the coordinate system. The resulting steady-state properties are also independent of the size of the calculation region, provided that the size is large compared to the mean free path between impacts (Wisdom and Tremaine (1988), Salo (1991)). Implicitly it is assumed in the local method that the rings are homogeneous on a scale comparable or larger than the size of the simulation region.

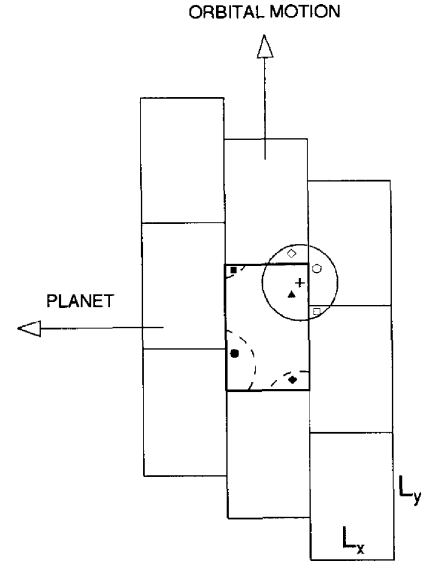


**Figure 1.3** Schematic diagram displaying the simulation cell (thick lines) and its eight surrounding replicas (thin lines). Gravitational forces on the given target particle (marked by cross) are calculated from the particles whose nearest images lie within a given maximum distance marked by the circle. The nearest image can either be the actual particle (solid symbols) or one of its copies (open symbols). Likewise, collisional calculations take into account impacts with image particles.

For a system of  $N$  particles moving according to Eqs. (1.4) the quantities

$$\begin{aligned} U &= \frac{1}{m_{tot}} \sum_{i=1}^N m_i \dot{x}_i, \\ V &= \frac{1}{m_{tot}} \sum_{i=1}^N m_i (\dot{y}_i - s x_i), \end{aligned} \quad (1.9)$$

are the analogues to centre-of-mass velocities, where  $m_{tot}$  is the total mass. From Eqs. (1.4),

$$\begin{aligned} m_{tot}(\dot{U} - 2\Omega V) &= \sum_i \sum_j F_x^{ij}, \\ m_{tot}(\dot{V} + (2\Omega + s)U) &= \sum_i \sum_j F_y^{ij}, \end{aligned} \quad (1.10)$$

where  $\vec{F}^{ij}$  stands for the mutual impact or gravity force, exerted by particle  $j$  on particle  $i$ . Since the forces cancel pairwise, the sums on the right-hand sides vanish. Also,  $U$  and  $V$  are unaffected by boundary crossings. Thus,  $U$  and  $V$  remain zero at all times if they vanish initially. This provides an useful check for the accuracy of the orbit and impact calculations. In the more general case,  $U$  and  $V$  oscillate about their initial values, but as shown in Wisdom and Tremaine (1988), the evolution of a system with arbitrary  $U_0$  and  $V_0$  is easily determined from the evolution with  $U_0 = V_0 = 0$ .

Eqs. (1.4) have the energy integral (multiply with velocities and integrate once),

$$\begin{aligned} E &= \sum_i m_i \left( \frac{1}{2} (\dot{x}_i^2 + \dot{y}_i^2 + \dot{z}_i^2) + \Omega s x_i^2 + \frac{1}{2} \Omega_z^2 z_i^2 \right) \\ &\quad - \frac{1}{2} \sum_i \sum_{j \neq i} G \frac{m_i m_j}{|\vec{r}_j - \vec{r}_i|}, \end{aligned} \quad (1.11)$$

the last term representing the self-gravitational potential energy (we have assumed that the additional forces arise from mutual self-gravity). In contrast to centre-of-mass velocities, the quantity  $E$  does not remain constant in boundary crossings or impacts.

## 1.3 Impact calculations

### 1.3.1 Instantaneous Impacts

In most local simulations (Wisdom and Tremaine (1988), Salo (1991, 1992b,a); Richardson (1993)) an impact model with instantaneous velocity changes has been used. This is well justified, as the contact time in impacts is probably less than one second (Bridges et al., 1984), or of the order of  $10^{-5}$  orbital periods. The damping of the relative velocity between a particle pair in the direction perpendicular to the impact plane is specified by the normal coefficient of restitution  $\varepsilon_n$ , describing the energy loss due to irreversible deformations during the impact. Similarly, the tangential coefficient of restitution,  $\varepsilon_t$ , can be included, describing the change of the relative velocity component along the impact plane. In this case the exchange of energy with the particles'

spin motion needs also be taken into account. Surface irregularities and the overall non-spherical shape of the particles may also affect the impact outcome. Below we summarize the equations for the velocity and spin changes in impacts, following from the specified elastic model and the conservation laws of linear and angular momentum. The equations are first derived in an inertial frame, and then we discuss the slight modifications required when a local rotating frame is used.

#### 1.3.1.1 Contact dynamics

The pre-collisional position, velocity and spin vector of the impacting particle are denoted by  $\vec{r}$ ,  $\dot{\vec{r}}$ , and  $\vec{\omega}$ , respectively, and its radius and mass by  $R$  and  $m$ . The impact partner is distinguished by the subscript 1, and the post-collisional quantities by a prime. We define

$$\begin{aligned} \vec{v} &= \dot{\vec{r}}_1 - \dot{\vec{r}}, \\ \vec{k} &= \frac{\vec{r}_1 - \vec{r}}{R + R_1}, \end{aligned} \quad (1.12)$$

standing for the velocity difference of the particle centres, and for the unit vector in the direction joining the particle centres. For an impact  $\vec{v} \cdot \vec{k} < 0$ . The pre-collisional velocity difference at the contact point, taking into account the spins, is

$$\vec{g} = (\dot{\vec{r}}_1 - R_1 \vec{\omega}_1 \times \vec{k}) - (\dot{\vec{r}} + R \vec{\omega} \times \vec{k}) \quad (1.13)$$

$$= \vec{v} - (R \vec{\omega} + R_1 \vec{\omega}_1) \times \vec{k}. \quad (1.14)$$

The post-collisional contact velocity  $\vec{g}'$  is determined by the impact model, giving its components in three orthogonal directions  $\vec{k}$ ,  $\vec{k} \times (\vec{g} \times \vec{k})$ , and  $\vec{g} \times \vec{k}$ , of which the last two lay on the impact plane; unit vectors in these directions will be denoted by  $\vec{k}_T$  and  $\vec{k}_\gamma$ , respectively. Note that these vectors form a right-handed system. We use the notation

$$\vec{g}' = -\varepsilon_n \vec{k} \vec{k} \cdot \vec{g} + \varepsilon_t \vec{k} \times (\vec{g} \times \vec{k}) + \varepsilon_\gamma \vec{g} \times \vec{k}, \quad (1.15)$$

which implies

$$\begin{aligned} \vec{k} \cdot \vec{g}' &= -\varepsilon_n \vec{k} \cdot \vec{g}, \\ \vec{k} \times (\vec{g}' \times \vec{k}) &= \varepsilon_t \vec{k} \times (\vec{g} \times \vec{k}) + \varepsilon_\gamma \vec{g} \times \vec{k} \end{aligned} \quad (1.16)$$

Thus  $\varepsilon_n$  denotes the coefficient of normal restitution, and if  $\varepsilon_\gamma = 0$ , then  $\varepsilon_t$  corresponds to friction. For totally elastic impacts  $\varepsilon_n = 1$  while with  $\varepsilon_n = 0$  the postcollisional perpendicular velocity difference vanishes. Similarly  $\varepsilon_t = 1$  means a frictionless impact while if  $\varepsilon_t = 0$  the whole tangential velocity difference at the contact point is lost. Note that  $\varepsilon_n = \varepsilon_t = 0$  does not imply sticking of particles as the orbital motion is free to separate them. In principle,  $-1 \leq \varepsilon_t < 0$  is also physically meaningful, corresponding to reversal of tangential velocity difference (Shu and Stewart, 1985). A non-zero  $\varepsilon_\gamma$  can be used to describe the effect of surface irregularities, giving rise to a post-collisional velocity component perpendicular to both  $\vec{k}$  and  $\vec{g}$ . If included,  $\varepsilon_\gamma$  needs to be a random variable with a zero mean, and since surface irregularities affect also in the direction of  $\vec{k} \times (\vec{g} \times \vec{k})$ , a similar random component needs to be present in  $\varepsilon_t$ .

The collisional changes of particles' velocity and spin vectors,

$$\begin{aligned}\Delta\dot{\vec{r}} &= \dot{\vec{r}}' - \dot{\vec{r}}, & \Delta\dot{\vec{r}}_1 &= \dot{\vec{r}}'_1 - \dot{\vec{r}}_1, \\ \Delta\vec{\omega} &= \vec{\omega}' - \vec{\omega}, & \Delta\vec{\omega}_1 &= \vec{\omega}'_1 - \vec{\omega}_1\end{aligned}\quad (1.17)$$

are determined by the conservation of linear momentum

$$m\dot{\vec{r}}' + m_1\dot{\vec{r}}'_1 = m\dot{\vec{r}} + m_1\dot{\vec{r}}_1, \quad (1.18)$$

and the conservation of angular momentum

$$\begin{aligned}m\vec{r} \times \dot{\vec{r}}' + m_1\vec{r}_1 \times \dot{\vec{r}}'_1 + J\vec{\omega}' + J_1\vec{\omega}'_1 \\ = m\vec{r} \times \dot{\vec{r}} + m_1\vec{r}_1 \times \dot{\vec{r}}_1 + J\vec{\omega} + J_1\vec{\omega}_1\end{aligned}\quad (1.19)$$

where  $J$  and  $J_1$  denote the particles' moments of inertia. These equations can be written into more compact form

$$m\Delta\dot{\vec{r}} + m_1\Delta\dot{\vec{r}}_1 = 0 \quad (1.20)$$

$$m\vec{r} \times \Delta\dot{\vec{r}} + m_1\vec{r}_1 \times \Delta\dot{\vec{r}}_1 + J\Delta\vec{\omega} + J_1\Delta\vec{\omega}_1 = 0 \quad (1.21)$$

Together with the model for  $\vec{g}'$  (Eq. 1.15), the conservation laws provide nine conditions for the six post collisional velocity components and six spin components. The remaining three relations are obtained by determining how the change of spin is distributed between the two particles. Since the forces acting on both particles are identical except in their sign, the torques during the impact are proportional to the particle radii,

$$\frac{J\Delta\vec{\omega}}{R} = \frac{J_1\Delta\vec{\omega}_1}{R_1}. \quad (1.22)$$

To simplify the notations in solving the above set of 12 equations, Eqs. (1.15),(1.20) - 1.22), we define

$$\vec{q} \equiv R\vec{\omega}, \quad \vec{q}_1 \equiv R_1\vec{\omega}_1, \quad \vec{q}_s \equiv \vec{q} + \vec{q}_1, \quad (1.23)$$

$$J = \alpha m R^2, \quad J_1 = \alpha_1 m_1 R_1^2. \quad (1.24)$$

Thus  $\vec{q}$  denotes the surface velocity due to spin rotation, and  $\alpha$  describes the internal mass distribution of particles; for homogeneous spherical particles  $\alpha = \alpha_1 = 2/5$ . From Eqs. (1.20) and (1.22) we find

$$\Delta\dot{\vec{r}} = -\frac{m_1}{m+m_1} \Delta\vec{v}, \quad \Delta\vec{q} = \frac{m_1\alpha_1}{m\alpha+m_1\alpha_1} \Delta\vec{q}_s \quad (1.25)$$

$$\Delta\dot{\vec{r}}_1 = \frac{m}{m+m_1} \Delta\vec{v}, \quad \Delta\vec{q}_1 = \frac{m\alpha}{m\alpha+m_1\alpha_1} \Delta\vec{q}_s \quad (1.26)$$

Inserting these in Eq. (1.21), using  $\vec{r}_1 = \vec{r} + \vec{k}(R+R_1)$  yields

$$\Delta\vec{q}_s = m_{\text{eff}} \left( \frac{1}{m\alpha} + \frac{1}{m_1\alpha_1} \right) \Delta\vec{v} \times \vec{k} \equiv f \Delta\vec{v} \times \vec{k} \quad (1.27)$$

Here

$$m_{\text{eff}} = \frac{m_1 m}{(m+m_1)} \quad (1.28)$$

is the effective mass of the pair. In the case of particles with the same internal mass distribution the factor  $f$  reduces to  $f = 1/\alpha$ , which equals  $f = 5/2$  for homogeneous spheres. The change of the relative velocity at the point of contact can thus be written (from Eq. 1.14)

$$\begin{aligned}\Delta\vec{g} = \vec{g}' - \vec{g} &= \Delta\vec{v} - \Delta\vec{q}_s \times \vec{k} \\ &= \Delta\vec{v} + f \vec{k} \times (\Delta\vec{v} \times \vec{k})\end{aligned}\quad (1.29)$$

Solving for  $\Delta\vec{v}$  gives

$$\Delta\vec{v} = \Delta\vec{g} \cdot \vec{k}\vec{k} + (1+f)^{-1} \left( \Delta\vec{g} \cdot \vec{k}_T \vec{k}_T + \Delta\vec{g} \cdot \vec{k}_\gamma \vec{k}_\gamma \right), \quad (1.30)$$

and inserting the components of  $\Delta\vec{g}$  which follow from the impact model, Eq. (1.15),

$$\Delta\vec{g} = -(1+\varepsilon_n)\vec{g} \cdot \vec{k}\vec{k} + (\varepsilon_t - 1)\vec{k} \times (\vec{g} \times \vec{k}) + \varepsilon_\gamma \vec{g} \times \vec{k} \quad (1.31)$$

finally gives

$$\begin{aligned}\Delta\vec{v} = & - (1+\varepsilon_n)\vec{g} \cdot \vec{k}\vec{k} \\ & - \frac{2}{7} \left[ (1-\varepsilon_t)\vec{k} \times (\vec{g} \times \vec{k}) - \varepsilon_\gamma (\vec{g} \times \vec{k}) \right].\end{aligned}\quad (1.32)$$

We have used  $(1+f)^{-1} = \frac{2}{7}$ , the value for homogeneous spheres. From Eq. (1.27) we obtain

$$\Delta\vec{q}_s = \frac{5}{7} \left[ (1-\varepsilon_t)(\vec{g} \times \vec{k}) + \varepsilon_\gamma (\vec{k} \times (\vec{g} \times \vec{k})) \right]. \quad (1.33)$$

The changes for the individual particles are now obtained from Eqs. (1.25). Note that in the case with no friction ( $\varepsilon_t = 1$ ) nor irregularity ( $\varepsilon_\gamma = 0$ ), the changes of velocity are independent from spins and no change of spins occurs.

### 1.3.1.2 Energy dissipation

The total kinetic energy of a colliding pair of particles consists of translational and rotational parts

$$E = E_{kin} + E_{rot} = \frac{1}{2}(m\dot{\vec{r}}^2 + m_1\dot{\vec{r}}_1^2) + \frac{1}{2}(m\alpha\vec{q}^2 + m_1\alpha_1\vec{q}_1^2) \quad (1.34)$$

With the centre of mass velocity

$$\vec{v}_c = \frac{m\dot{\vec{r}} + m_1\dot{\vec{r}}_1}{m+m_1}, \quad (1.35)$$

the translational part can be written as

$$E_{kin} = \frac{1}{2} \left( (m+m_1)\vec{v}_c^2 + m_{\text{eff}}\vec{v}^2 \right), \quad (1.36)$$

and since  $\vec{v}_c$  is conserved,

$$\Delta E_{kin} = \frac{1}{2} m_{\text{eff}} \Delta(\vec{v}^2) \quad (1.37)$$

The rotational contribution can be decomposed in a similar manner by defining

$$\vec{q}_c = \frac{m\alpha\vec{q} - m_1\alpha_1\vec{q}_1}{m\alpha + m_1\alpha_1}, \quad (1.38)$$

leading to

$$E_{rot} = \frac{1}{2} \left[ (m\alpha + m_1\alpha_1)\vec{q}_c^2 + \frac{m_{\text{eff}}}{f} \vec{q}_s^2 \right]. \quad (1.39)$$

Since  $\vec{q}_c$  is conserved, we have

$$\Delta E_{rot} = \frac{1}{2} \frac{m_{\text{eff}}}{f} \Delta(\vec{q}_s^2), \quad (1.40)$$

As  $\Delta\vec{q}_s = f\Delta\vec{v} \times \vec{k}$ , the total energy change is

$$\begin{aligned}\Delta E &= \frac{1}{2} m_{\text{eff}} \left[ 2\vec{v} \cdot \Delta\vec{v} + (\Delta\vec{v})^2 + 2\Delta\vec{v} \times \vec{k} \cdot \vec{q}_s + f(\vec{k} \times \Delta\vec{v})^2 \right] \\ &= \frac{1}{2} m_{\text{eff}} \left[ 2\vec{g} \cdot \Delta\vec{v} + (\Delta\vec{v})^2 + f(\vec{k} \times \Delta\vec{v})^2 \right].\end{aligned}\quad (1.41)$$

Inserting  $\Delta\vec{v}$  from Eq.(1.30) gives

$$\Delta E = -\frac{1}{2}m_{\text{eff}} \left[ \Delta(g_n^2) + \frac{1}{1+f} \Delta(g_t^2) \right] \quad (1.42)$$

where  $g_n \equiv |\vec{g} \cdot \vec{k}|$  and  $g_t \equiv |\vec{k} \times (\vec{g} \times \vec{k})|$ . In terms of the impact model we find

$$\Delta E = -\frac{1}{2}m_{\text{eff}} \left[ (1 - \varepsilon_n^2) g_n^2 + \frac{1}{1+f} \left( 1 - (\varepsilon_t + \varepsilon'_\gamma)^2 - \varepsilon_\gamma^2 \right) g_t^2 \right], \quad (1.43)$$

where we have also explicitly included the random component  $\varepsilon'_\gamma$  present in  $\varepsilon_t$ . Note that the factor  $\frac{1}{1+f}$  enters by including the exchange of energy between rotational and translational motions. The use of  $\varepsilon_t$  to account for friction without including particle spins, would correspond to setting  $f = 0$ , thus leading to incorrect amount of dissipation.

### 1.3.1.3 Surface irregularities

In principle, irregularities can be described in terms of  $\varepsilon_\gamma$ , but this treatment has some caveats. Namely, for a realistic impact model  $\Delta E \leq 0$ . With  $\varepsilon_\gamma = \varepsilon'_\gamma = 0$  the energy change implied by Eq. (1.43) is guaranteed to be negative for all  $0 < \varepsilon_n < 1, -1 < \varepsilon_t < 1$ , but if irregularity is included, the allowed range of  $\varepsilon_\gamma$  and  $\varepsilon'_\gamma$  depends on  $\varepsilon_n, \varepsilon_t$ , and the ratio  $g_n/g_t$ . This makes it hard to interpret the physical meaning of the model. An alternative description for small-scale irregularity was introduced in (Salo, 1987a,b), where the actual normal vector of the impact plane,  $\vec{k}^*$ , is allowed to deviate from  $\vec{k}$  by a small random amount in each impact,

$$\vec{k}^* = \vec{k} \sqrt{1 - \gamma_a^2 - \gamma_b^2} + \gamma_a \vec{k}_T + \gamma_b \vec{k}_\gamma, \quad (1.44)$$

where  $\gamma_a$  and  $\gamma_b$  are random variables with zero mean, and using

$$\Delta\vec{g} = -(1 + \varepsilon_n)\vec{g} \cdot \vec{k}^* \vec{k}^* + (\varepsilon_t - 1)\vec{k}^* \times (\vec{g} \times \vec{k}^*). \quad (1.45)$$

On the other hand, the overall shape of the particles is assumed to stay close to spherical, so that Eq. (1.14) can still be used for the relative velocity at the contact point. The advantage of this description is that the variables  $\gamma_a$  and  $\gamma_b$  have an obvious physical interpretation, and a negative energy loss is guaranteed for any allowed impact with  $\vec{k}^* \cdot \vec{v} < 0$ .

### 1.3.1.4 Rotating frame

The calculations presented above are valid in an inertial frame. When using a rotating frame, with same instantaneous axis directions, the velocities and spins are connected to their inertial frame values as

$$\begin{aligned} \dot{\vec{r}}_I &= \dot{\vec{r}}_\Omega + \vec{\Omega} \times \vec{r}_I, \\ \dot{\vec{\omega}}_I &= \dot{\vec{\omega}}_\Omega + \vec{\Omega}, \end{aligned} \quad (1.46)$$

where subscripts  $I$  and  $\Omega$  are used to distinguish between the two frames. On the other hand, the instantaneous direction vectors are unaffected. Thus the only differences to

Eqs. (1.32) and (1.33) for  $\dot{\vec{r}}^*$  and  $\Delta\omega$  would come through  $\vec{g} = \vec{v} - (R_1\vec{\omega}_1 + R\vec{\omega}) \times \vec{k}$ . However, as

$$\begin{aligned} \vec{v}_I &= \vec{v}_\Omega + \vec{\Omega} \times \vec{k}(R + R_1), \\ (R\vec{\omega} + R_1\vec{\omega}_1)_I \times \vec{k} &= (R\vec{\omega} + R_1\vec{\omega}_1)_\Omega \times \vec{k} \\ &\quad + (R + R_1)\vec{\Omega} \times \vec{k}, \end{aligned} \quad (1.47)$$

the vector  $\vec{g}$  has the same expression in both frames. Thus no modifications are needed if both, velocities and spins, are treated consistently. Alternatively, we may use  $\vec{\omega}_I$  in the collisional equations and add a correction term  $(R + R_1)\Omega \times \vec{k}$  to  $\vec{g}_\Omega$ , as was done in Hämeen-Anttila and Salo (1993).

### 1.3.2 Force model for impacts

The treatment of impacts in terms of instantaneous velocity changes leads to problems if the particles do not separate after the impact. Even in the absence of mutual gravity, a situation can occur where the particles' have a net central acceleration toward each other even when their post-collisional relative velocity is zero. This corresponds to a sliding motion of the particles, before they are eventually separated by the shear. Following Wisdom and Tremaine (1988) such a phase can be described in terms of a succession of small jumps, achieved by setting  $\varepsilon_n = 1$  whenever the perpendicular impact velocity falls below a threshold value, say,  $0.01R\Omega$ . Since such impacts do not dissipate much energy to start with, the energy balance of the system is not affected by this replacement.

However, the problem becomes more severe if self-gravity or cohesive forces between particles are included. In these cases impacts may lead to a semi-permanent physical sticking of particles. In the instantaneous impact method this leads to particle overlaps, unless some special measure is applied to force a separation of the particles. Further difficulties may still arise for example if gravitational aggregates are formed, in which case it is insufficient to consider only binary impacts independently from each other. A physically motivated solution, which is also computationally feasible, is to include explicitly the pressure forces affecting the particles in the impact. In Salo (1995) this was done in terms of the linear visco-elastic model originally developed by Dillely (1993) for the theoretical parameterisation of his measurements of velocity and size-dependent elasticity. Likewise, frictional forces may be included in the simulations (Salo, 1995; Morishima and Salo, 2006). Such *Discrete element method (DEM)* algorithms Cundall and Strack (1979) are commonly used in granular dynamics (see e.g. Pöschel and Schwager (2005)).

The equations of motion for the impacting particles are

$$\begin{aligned} m\ddot{\vec{r}} &= \vec{F}^{\text{imp}} + \vec{F} \\ m_1\ddot{\vec{r}}_1 &= \vec{F}_1^{\text{imp}} + \vec{F}_1, \end{aligned} \quad (1.48)$$

$$\begin{aligned} J\dot{\vec{\omega}} &= R\vec{k} \times \vec{F}^{\text{imp}} \\ J_1\dot{\vec{\omega}}_1 &= R_1(-\vec{k}) \times \vec{F}_1^{\text{imp}} \end{aligned} \quad (1.49)$$

where  $\vec{F}_1^{\text{imp}} = -\vec{F}^{\text{imp}}$  represent the impact forces, and  $\vec{F}$  and  $\vec{F}_1$  include additional forces affecting the particles

(central force and gravity of other particles), not causing any torque on the impacting pair. Let us express the impact force as

$$\vec{F}_1^{imp} = f_N \vec{k} + f_T \vec{k}_T \quad (1.50)$$

with the normal force (the tangential force  $f_T$  will be treated below)

$$\begin{aligned} f_N(\xi) &= \beta_1 \xi + \beta_2 \dot{\xi}, & \xi > 0 \\ &= 0, & \xi \leq 0 \end{aligned} \quad (1.51)$$

where

$$\xi = R + R_1 - |\vec{r} - \vec{r}_1| \quad (1.52)$$

is the penetration depth during the impact. Here  $\beta_1 > 0$  is the spring constant of the restoring harmonic force, while due to the dissipative term with  $\beta_2 > 0$  the energy stored during the compression phase is not completely returned in rebound phase. From Eqs. (1.48), (1.51) and (1.52),

$$\begin{aligned} \dot{\xi} &= -\vec{v} \cdot \vec{k}, \\ \ddot{\xi} &= -\vec{v} \cdot \dot{\vec{k}} - \vec{v} \cdot \ddot{\vec{k}}, \\ \ddot{\vec{v}} &= (\vec{F}/m - \vec{F}_1/m_1) + \vec{F}_1^{imp}/m_{\text{eff}}, \end{aligned} \quad (1.53)$$

which yields

$$\ddot{\xi} = -\frac{(\beta_1 \xi + \beta_2 \dot{\xi})}{m_{\text{eff}}} + C, \quad (1.54)$$

with

$$C = \left( \frac{\vec{F}_1}{m_1} - \frac{\vec{F}}{m} \right) \cdot \vec{k} - \vec{v} \cdot \ddot{\vec{k}}, \quad (1.55)$$

where  $C$  contains the difference of additional accelerations felt by the particles, as well as the change of the normal direction during the impact.

Ignoring the term  $C$ , the solutions of Eq. (1.54) are exponentially damped oscillations (impact starts at  $t = 0$  when  $\xi = 0$ ),

$$\xi = \frac{v_n}{\omega} \exp(-\omega_d t) \sin(\omega t) \quad (1.56)$$

where  $v_n \equiv \dot{\xi}(0)$ , and the oscillation frequency  $\omega$  and the damping rate  $\omega_d$  are

$$\begin{aligned} \omega^2 &= \omega_0^2 - \omega_d^2, \\ \omega_0^2 &= \frac{\beta_1}{m_{\text{eff}}}, \\ \omega_d &= \frac{1}{2} \frac{\beta_2}{m_{\text{eff}}}, \end{aligned} \quad (1.57)$$

with  $\omega_0$  denoting the undamped frequency. The duration of the impact (the length of the first half-cycle) and the coefficient of restitution are

$$\begin{aligned} T_{dur} &= \pi/\omega \approx \pi/\omega_0 \\ \varepsilon_n &= -\frac{\dot{\xi}(T_{dur})}{\dot{\xi}(0)} = \exp\left(-\pi \frac{\omega_d}{\omega}\right) \end{aligned} \quad (1.58)$$

Thus specifying  $\beta_1/m_{\text{eff}}$  gives the approximate impact duration, and then  $\beta_2$  is determined by  $\varepsilon_n$ ,

$$\frac{\beta_2}{m_{\text{eff}}} = \frac{2\omega_0}{\sqrt{\left(\frac{\pi}{\ln \varepsilon_n}\right)^2 + 1}}. \quad (1.59)$$

Note that a velocity-dependent elasticity law  $\varepsilon_n(v_n)$  can also be used in simulations: in this case the value of  $\beta_2$  is chosen for each impact based on the pre-impact relative velocity  $v_n$  of the pair and the desired  $\varepsilon_n$ .

In the force method the particle motion is integrated through the impact, so that the time step is basically determined to be a small fraction of  $T_{dur}$ . On the other hand, the total span of any simulation is determined by the orbital time-scale  $T_{per} = 2\pi/\Omega$ . Since  $T_{dur} \ll T_{per}$  is advantageous to speed up the calculations by scaling the simulated impact duration to be larger than the physical duration. Otherwise most of the computing time is spent on calculating the motion of particles which are not currently colliding with much smaller steps than required to resolve their motion due tidal and self-gravitational forces. Indeed, the most attractive feature of the above linear force model is that the impact duration is independent of impact velocity, and is easily adjusted via  $\beta_1$ .

However, there is an upper limit for the allowed  $T_{dur}$ , as the solution obtained above ignored the term  $C$ : preserving this term may change the implied elasticity. Also, in the case the impact duration is extended to  $T_{dur} > 1/\omega_c$ , where  $\omega_c$  is the impact frequency, the binary nature of collisions is not retained. It is thus important to address what is the maximum  $T_{dur}$  one can use. According to simulation tests (see Fig. 1.4), using  $T_{dur}/T_{per} < 10^{-2}$  leads to a practically same steady state as the instantaneous impact method. Most of the simulations of Sect. 1.8.2 and use  $\omega_0/\Omega = 400$ , corresponding to  $T_{dur}/T_{per} = 1/800$ .

### 1.3.2.1 Surface friction

A straightforward way to include friction to the force model is to use

$$f_T = \mu f_N \quad (1.60)$$

in Eq. (1.51), where  $\mu < 0$  denotes the coefficient of friction. This description is quite different from using  $\varepsilon_t$  in the instantaneous impact model, as there is no single choice of  $\mu$  that would correspond to a given  $\varepsilon_t$ . To connect  $\mu$  to  $\varepsilon_t$ , we may use  $\vec{g}$  from Eqs. (1.48) and (1.49)

$$\begin{aligned} \vec{g} &= \vec{v} - (R_1 \dot{\vec{w}}_1 + R \dot{\vec{w}}) \times \vec{k} \\ &= \frac{1}{m_{\text{eff}}} \left( \vec{F}_1^{imp} + f \vec{k} \times (\vec{F}_1^{imp} \times \vec{k}) \right) \\ &= \frac{1}{m_{\text{eff}}} \left( f_N \vec{k} + (1+f)\mu f_N \vec{k}_T \right) \end{aligned} \quad (1.61)$$

where  $f$  is the factor defined in connection to Eq. (1.29), reducing to 5/2 for homogeneous spheres; we have ignored here the extra forces due to orbital motion and self-gravity ( $C = 0$ ). Thus, the total change of normal and tangential velocity difference are

$$\begin{aligned} \Delta g_n &= \Delta \vec{g} \cdot \vec{k} = \int_{T_{dur}} \frac{f_N}{m_{\text{eff}}} dt \equiv (1 + \varepsilon_n) g_n \\ \Delta g_t &= \Delta \vec{g} \cdot \vec{k}_T = \frac{7}{2} \mu \int_{T_{dur}} \frac{f_N}{m_{\text{eff}}} dt \equiv (\varepsilon_t - 1) g_t \end{aligned} \quad (1.62)$$

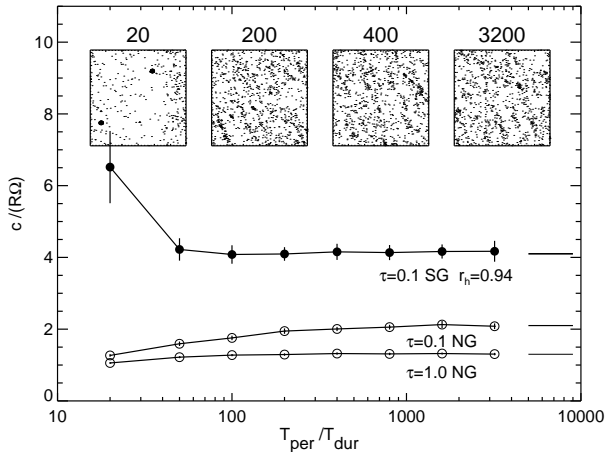


**Figure 1.4** The steady-state velocity dispersion in force-method simulations using different impact durations  $T_{dur}$ . Results with instantaneous impact method are indicated by the horizontal lines. A constant  $\varepsilon_n = 0.5$  is used. In the non-gravitating simulation (NG) elongation of impact duration ( $T_{per}/T_{dur} \lesssim 100$ ) enhances dissipation, resulting in a lower velocity dispersion. In self-gravitating simulations (SG) this extra dissipation is compensated by the enhanced energy gain due to gravitational viscosity for ( $T_{per}/T_{dur} \lesssim 50$ ), caused by the longer time the particles spend in the vicinity of each other. For long enough  $T_{dur}$  the particles may even stick together, leading to strongly enhanced gravitational viscosity. The inserts show snapshot from the self-gravitating simulations with different  $T_{per}/T_{dur}$  ratios.

where the force model results are identified with those of the instantaneous impact model. Thus

$$\varepsilon_t = 1 + \frac{7}{2}\mu(1 + \varepsilon_n)g_n/g_t \quad (1.63)$$

implying  $\varepsilon_t \leq 1$  since  $\mu < 0$ . Nevertheless, the regime  $\varepsilon_t < 0$  can not be modeled, as the frictional force always acts against the relative tangential contact velocity. In practice, if friction is strong enough to suppress the tangential velocity difference,  $g_t = 0$  appears as a discontinuity in the force and the solution oscillates around  $\varepsilon_t = 0$ .

In principle, more realistic theoretical models for both friction and normal restitution (Spahn et al., 1995) can also be used in simulations, but then the various scalings become more complicated, as the impact duration will generally depend on the impact velocity.

### 1.3.3 Search of impact pairs

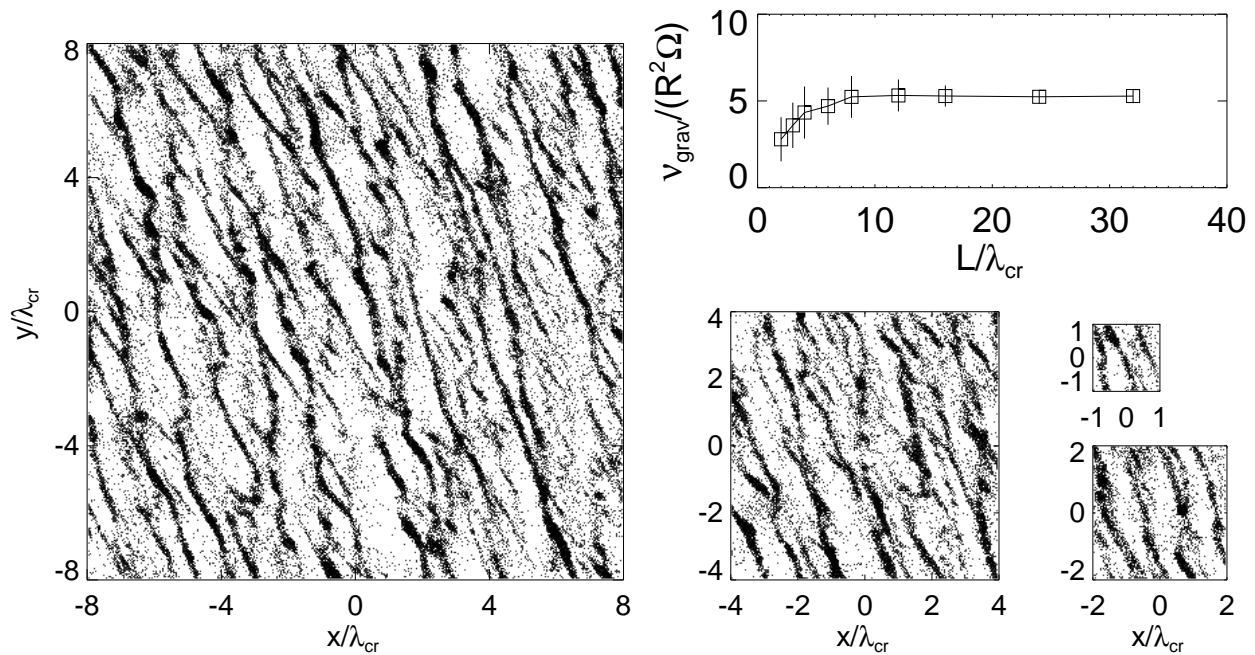
The speed of the collisional simulation depends crucially on the efficient search of impact pairs. For example, in their simulations of non-gravitating particles Wisdom and Tremaine (1988) used the fact that orbits between impacts are Keplerian epicycles, and solved iteratively for the intersection time of each pair of epicycles. The impact of the pair with the smallest impact time was executed with instantaneous velocity changes, and the post-impact orbital elements were calculated, leading to updated intersection times with all the other particles. The system was thus moved on from one

impact to the next (the method is called “event-driven”). Similar methods were used also in the early simulations of rarefied azimuthally complete rings: due to extremely long intervals between impacts elaborate schemes were developed for detecting orbital intersections taking place after even several hundreds of synodic periods (Hämeen-Anttila and Lukkari, 1980).

Event-driven methods are fairly fast for small particle numbers ( $N \approx 50$  in Wisdom and Tremaine (1988)), but as  $N$  increases, the checking of next orbital intersections between all  $N(N-1)/2$  pairs gets excessively slow. Also, the inclusion of additional forces besides the central gravity poses problems. Therefore, in the self-gravitating case the equations of motions are integrated with small time steps, and the potential intersections during each step are searched only among the neighboring particles. Similar stepwise time integration is advantageous also in the case of high particle density and large  $N$ , even if self-gravity is not included. Provided that the step size is small, the distances between particles can be expanded as a second-order Taylor polynomial, providing a fast method for constructing a list of potential impacts during the step (Salo, 1991). From this list, the impacts during the time step are then executed as in the event-driven method.

Regardless of the time-advancement method a considerable speedup can be achieved if the number of pairs examined for potential impacts is kept as small as possible. This can be done quite efficiently by keeping track of the maximum pre-step separation which has actually led to an impact during previous steps, and by checking in each step only those pairs whose distance does not exceed this maximum, multiplied by some threshold factor. This threshold must be chosen in a manner which ensures that no impacts are lost, and it also must be dynamically adjusted as the velocity dispersion of the system evolves. In the optimal case, the number of pairs examined is proportional to  $\sqrt{v^2}/(R\Omega)N$ . Note that the actual orbital integration needs not to be performed by a Taylor-series: for example in Salo (1992a) a fourth order Runge-Kutta integration was utilized, and the impact locations initially estimated by the second-degree polynomial expansion were iteratively improved to correspond to the full accuracy of the integration.

It must be stressed that it is important to take correctly into account impacts taking place over boundaries of the local calculation region. For small calculation regions this fraction can be quite significant, and the omission of such impacts will considerably modify the energy balance, and thus, all steady-state properties of the system. Also, if the force method is used, even a single non-detected impact may lead to large injection of energy to the system if it leads to a deep overlap on the next step. However, such a situation is easy to detect and correct.



## 1.4 Calculation of self-gravity

### 1.4.1 Force evaluation

Inclusion of gravitational forces increases the computational burden significantly, as in principle the forces between each particle pair need to be included (as well as to account for the contribution of the replicas of the local calculation region). Moreover, self-gravity typically enhances the velocity dispersion and increases the impact frequency (see Section 1.8). Both factors make the collisional calculations more time consuming. These problems are especially pronounced in the case of a weak tidal field, i.e. far from the planet, when gravitationally bound particle aggregates form. Proper simulation of self-gravity also sets additional constraints for the required minimum size of the calculation region, since it must exceed the scale of the self-gravity wake structures formed via gravity (roughly a few times Toomre critical wavelength  $\lambda_{cr}$ , see Fig 1.5). In practice this means using at least  $10^4 - 10^5$  simulation particles. On the other hand, for non-gravitating spatially uniform systems a fairly modest particle number ( $10^2 - 10^3$ ) is usually sufficient to give the steady-state properties with a good accuracy.

The most straight-forward way of force evaluation is the *particle-particle (PP)* method, using a direct summation over particle pairs. The obvious advantage is that no approximations are involved, the gravitational field corresponding exactly to that implied by the particle ensemble. The method can also be fairly efficient (Daisaka et al., 2001) when using a special-purpose processor, like GRAPE, with a hardware calculation of gravity forces (Makino and Fujino, 1993). With standard-type processors the implied  $N^2$  time consumption becomes however prohibitively large al-

**Figure 1.5** Snapshots of self-gravitating simulations with different sized calculation regions, after 50 orbital periods. In each simulation  $\tau = 0.5$ ,  $\varepsilon_n = 0.5$ ,  $\rho = 900 \text{ kg/m}^3$ ,  $R = 1 \text{ m}$ , and  $a = 100,000 \text{ km}$  ( $r_h = 0.82$ ). The width of the square-shaped region is  $L/\lambda_{cr} = 32, 16, 8, 4, 2$ . In physical units the Toomre critical wavelength  $\lambda_{cr} = 41.6 \text{ m}$ . The self-gravity is calculated from all particles within a cylindrical radius  $\Delta_{max} = L/2$ . Gravitational forces from within  $\Delta_{min} = 0.25\lambda_{cr}$  are calculated with the PP-method and beyond that with the PM-method, using a grid spacing of  $\lambda_{cr}/16$ . The graph shows the gravitational viscosity (Eq. 1.85) as a function  $L/\lambda_{cr}$  (average between 25-50 orbits).

ready for a few thousand particles, so that other methods are needed. Also, due to partial cancellation of distant forces it is in fact unnecessary to calculate the contribution from distant particles with the same accuracy as that of the nearby particles.

This fact is utilized in *hierarchical tree-codes*, where the distant particles are grouped together in force calculation, so that only few low order moments of their distribution are included (??). The essential part of the method is the efficient construction of the connected particle lists ('tree'), leading to a  $N \ln N$  dependence of the CPU-time consumption. Richardson (1994) first applied this method to self-gravitating rings. On the other hand, N-body simulations of galactic dynamics often employ *particle-mesh (PM)* method (see Sellwood 2015): the density of the system is tabulated in a regular mesh, and the forces (or gravity potential) at each mesh location are evaluated by convolving the density with the interaction law, and then interpolating to the particle locations. The speed of the method relies on the use of a Fast Fourier Transform for performing the force convolution, and in the optimal case the CPU-time consumption of gravity calculations is determined mainly by the inter-

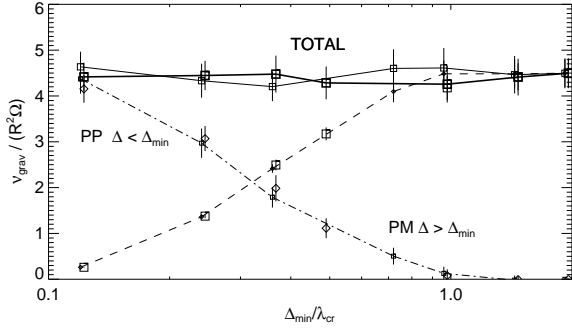


**Figure 1.6** The near (PP) and far (PM) contributions to self-gravity, measured in terms of gravitational viscosity, are compared for different dividing distances  $\Delta_{min}$ . Simulation parameters are the same as in the previous figure, and the total extent of the simulation region is  $4\lambda_{cr} \times 4\lambda_{cr}$ . The rightmost point corresponds to using solely PP method. Two set of simulations are shown, with  $\lambda_{cr}/16$  (thin lines, small symbols) and  $\lambda_{cr}/32$  (thick lines, large symbols) PM grid spacing. Within error bars, the total gravitational viscosity is the same in all simulations.

polation of forces, being linear in  $N$ . In current large-scale cosmological simulations the tree and PM methods are often combined (Springel, 2005).

The important difference between planetary rings and galaxy disks is that binary gravitational encounters between ring particles are not insignificant compared to the mean gravitational field (rings are not 'collisionless'). Therefore the smoothing of forces implied by the gravity mesh (or by explicit gravity softening) is incorrect. On the contrary, the most important contributions from self-gravity come from the fluctuating gravitational forces exerted by the nearest neighboring ring particles (within  $\sim \lambda_{cr}$ , see Fig. 1.7).

An obvious way to speed up the calculations, while retaining the accurate treatment of nearby gravity encounters, is to combine PP and PM methods, for example in a manner that was employed in Salo et al. (2001). In this treatment the gravitational force exerted on each particle is divided in a nearby and distant contribution,

$$\vec{F}_i = \vec{F}_i^{near} + \vec{F}_i^{far},$$

$$\vec{F}_i^{near} = G \sum_{\Delta_{ij} < \Delta_{min}} m_j \frac{\vec{r}_j - \vec{r}_i}{|\vec{r}_j - \vec{r}_i|^3}, \quad (1.64)$$

$$(1.65)$$

$$\vec{F}_i^{far} = G \int_{\Delta > \Delta_{min}} \rho(\vec{r}) \frac{\vec{r} - \vec{r}_i}{|\vec{r} - \vec{r}_i|^3} d^3r,$$

where  $\Delta$  denotes the projected 2D distance in the  $xy$ -plane. The near contribution is calculated by direct particle-particle summation, in order to include accurately the effects of close gravitational encounters, as well as the gravitational sticking of particles. Typically  $\Delta_{min} \ll L_x, L_y$ , so that just a few percents of all  $N(N-1)/2$  particle pairs are involved. The latter, usually smaller distant contribution is calculated with a particle-mesh method.

An efficient way to calculate the PM contribution is to use FFT in a sheared coordinate system, defined by the transformation

$$\begin{aligned} u &= x, \\ v &= y - stx, \end{aligned} \quad (1.66)$$

where  $s = -\frac{3}{2}\Omega$  in the Keplerian case. In these coordinates the Eqs. (1.8) for the image particles transform into

$$\begin{aligned} u' &= u + nL_x, \\ v' &= v + mL_y. \end{aligned} \quad (1.67)$$

indicating that the system is double periodic in the planar directions. We define a 3D Cartesian mesh with  $m_u \times m_v \times m_z$  cells, and tabulate the mass  $\delta m(u, v, z)$  in each cell by a cloud-in-cell (CIC) assignment. In planar directions the mesh has the same size as the calculation region,  $|u| < L_x/2, |v| < L_y/2$ . The vertical coverage of the mesh,  $|z| < L_z/2$  is tied to the vertical thickness of the system, using  $L_z/2 = k\sqrt{z^2}$ , for example with  $k = 3$ : the small fraction of particles with  $|z| > L_z/2$  contribute insignificantly to the total density and can be ignored. The force on each cell center is obtained with a convolution

$$\vec{F}_{i,j,k} = G \sum_{l,m,n} \delta m_{l,m,n} \vec{\Gamma}_{l-i,m-j,n-k} \quad (1.68)$$

where  $\vec{\Gamma}$  (with same dimensions as  $\delta m$ ) denotes the Green function for the gravitational interaction between the cells. Written in terms of the newly defined coordinates,

$$\vec{\Gamma}_{abc} = (a\Delta u, b(\Delta v + st\Delta u), c\Delta z) / d_{abc}^3 \quad (1.69)$$

with

$$d_{abc} = ((a\Delta x)^2 + (b(\Delta v + st\Delta u))^2 + (c\Delta z)^2)^{1/2}. \quad (1.70)$$

To exclude the near contribution  $\Gamma_{abc}$  is set to zero for  $(a\Delta x)^2 + (b(\Delta v + st\Delta u))^2 < \Delta_{min}^2$ .

If carried out by direct summation, the convolution in Eq. (1.68) would require  $\propto (m_x m_y m_z)^2$  operations. Even for moderate spatial resolution this would mean an excessive number of calculations (even larger than that for the direct summation over all  $N(N-1)/2$  pairs). It is therefore essential to utilize the Fourier convolution theorem, according to which the inverse transform of mesh forces equals the product of the inverse transforms of density and Green function,

$$\vec{\tilde{F}}_{i,j,k} = \vec{\tilde{\delta m}}_{l,m,n} \vec{\tilde{\Gamma}}_{l-i,m-j,n-k}. \quad (1.71)$$

In order to be able to apply the convolution theorem, we double the mesh size in the vertical direction, padding the extra cells with zeros. Using Fast Fourier Transform, the number of calculations becomes proportional to  $(m_x \ln m_x)(m_y \ln m_y)(2m_z \ln 2m_z)$ , making the method feasible. The forces at the particle locations are interpolated from the grid, with the same CIC-assignment as in the tabulation of density. The forces on the few particles with  $|z| > L_z/2$  are calculated with an extrapolation from the grid. In this manner the force on each particle is due to the density in the region which corresponds in size to the whole original

rectangular calculation region (see Fig. 1.3). If a circular region is desired (to avoid any artificial 'polarization' of forces due to corners of the region) we can set the green function to zero beyond some distance  $\Delta_{max} < \max\{L_x/2, L_y/2\}$ .

Figure 1.6 shows the gravitational viscosity (Eq. (1.85)) from  $4\lambda_{cr} \times \lambda_{cr}$  simulations where different dividing distances  $\Delta_{min}$  between PP and PM methods are used, confirming that similar results are obtained in all cases. However, the gravity calculation is about 10 faster when using PP+PM with  $\Delta_{min}/\lambda_{cr} = 1/8$  in comparison with using just the PP method to calculate gravity from within  $2\lambda_{cr}$ . For larger calculation regions and particle numbers, the gain in speed becomes even more important.

#### 1.4.2 Approximate treatments of self-gravity

Fully self-consistent calculation of particles' mutual gravity, as described above, is quite CPU time intensive. Wisdom and Tremaine (1988) devised a simple method for mimicking self-gravity in terms of an enhanced vertical frequency in the dynamical equations. It is based on writing  $\Omega_z^2 = \Omega^2(1 + F_z/F_c)$ , where  $F_z/F_c$  is the ratio between the vertical self-gravity and the vertical component of central force. Most of their simulations used a constant  $\Omega_z/\Omega = 3.6$  ( $F_z/F_c \approx 12$ ), approximating the enhancement in vertical gravity due self-gravity in the dense B-ring of Saturn. Such a treatment mimics qualitatively quite well the effects of vertical gravity, like the enhanced impact frequency (see Sect. 1.8), which leads to strongly increased non-local viscosity, thus promoting viscous overstability. Indeed, the use of  $\Omega_z/\Omega > 1$  is a very useful method for analyzing overstability, in terms of hydrodynamic transport coefficients evaluated from N-body simulations (Salo et al., 2001; Schmidt et al., 2001). Nevertheless, since the approximation ignores the planar components of gravity, which are responsible for the emergence of self-gravity wakes, it is questionable how useful it is for describing real systems in any quantitative way.

Another useful approximation can be applied to the calculation of axisymmetric component of self-gravity, in terms of a superposition of infinite plane waves. We first make a radial Fourier decomposition of the tangentially averaged surface density

$$\Sigma(x) = \Sigma_0 \left[ 1 + \sum_{m=1}^{\infty} A_m \cos \left( m \frac{2\pi}{L_x} (x - x_m) \right) \right], \quad (1.72)$$

where  $A_m$  and  $x_m$  are the fractional amplitude and phase of different m-components with wavelengths  $\lambda = L_x/m$ . We then treat each component as an infinite plane wave, and use Poisson equation for an infinite 2D sheet to calculate the corresponding radial force. Superposition of modes with different  $m$  gives

$$F_x(x) = -2\pi G \Sigma_0 \sum_{m=1}^{m_{max}} A_m \sin \left[ m \frac{2\pi}{L_x} (x - x_m) \right]. \quad (1.73)$$

A finite  $m_{max}$  can be used in order to suppress small scale noise. Such a treatment was applied in Salo and Schmidt

(2010) to compare viscous instability in N body simulations to Schmit and Tscharnuter (1995) hydrodynamic predictions in the case axisymmetric self-gravity is included.

#### 1.4.3 Time integration

In the force method the basic timestep of integration is determined by the need to resolve the rebound of individual particle pairs. Depending on the chosen spring constant of the restoring harmonic force, this requires time step of the order of  $\Delta T_{imp} = (0.01 - 0.1)T_{dur} \sim (10^{-4} - 10^{-5})T_{orb}$ , where  $T_{dur}$  is the impact duration. On the other hand, self-gravitational forces are practically constant over such sort time scales. To speed up calculations, one can therefore use a larger time step, say  $\Delta T_{grav} \sim 10^{-3}T_{orb}$ , for updating the gravity forces. This simple method works well in the case of gravity wake structures: the errors made in keeping the self-gravity constant tend to cancel each other on the average. However, when particles stick physically, this method may lead to artificial destabilization of gravity aggregates via rotational instability (Karjalainen and Salo, 2004). This is solely a numerical artifact, rising from the fact that the force integration errors do not cancel each other, but lead to a net torque on particles attached to the aggregate. As illustrated in Karjalainen and Salo (2004) a totally sufficient remedy is to calculate both the forces and their time derivatives at the beginning of each gravity step, and then apply linear extrapolation of self-gravity during the step. An even more accurate method would be to calculate the nearby PP gravity during each  $\Delta T_{imp}$  and update the particle-mesh gravity with longer intervals.

#### 1.5 Extracting quantities from simulations

The fundamental <sup>1</sup> quantity describing both the dynamics and observed structures of Saturn's rings is the dynamical (geometric) optical depth, defined as the total surface area of particles divided by the total area. For identical particles with radius  $R$

$$\tau = \frac{N\pi R^2}{L_x L_y}. \quad (1.74)$$

One of the main advantages of the local method is that the optical depth (and surface density in case of self-gravitating particles) of the system is fixed. Thus, after the establishment of local energy balance, all dynamical properties characterizing this density can be obtained with an arbitrary accuracy, by time averaging over sufficiently long time intervals over all particle orbits and impacts. The efficiency of time averaging was strikingly demonstrated in Wisdom and Tremaine (1988), who made a practically complete study

<sup>1</sup> Observationally the importance comes from the close correspondence of  $\tau$  to the normal photometric optical depth  $\tau_{phot}$ , which is the quantity inferred from occultation experiments: in the limit of homogeneous low filling factor systems  $\tau$  and  $\tau_{phot}$  are identical. However, in a typical case of non-homogeneous high filling factor rings they generally differ, see (Salo and Karjalainen, 2003; Salo et al., 2004; Porco et al., 2008; rob, n.d.).

of identical, non-gravitating particles, up to optical depths  $\sim 3$ , using experiments with only  $N = 50$  particles.

### 1.5.1 Steady-state quantities

The interesting dynamical quantities include the impact frequency  $\omega_c$ , the velocity dispersion tensor  $\widehat{C}_{\alpha\beta}$ , the pressure tensor  $\widehat{P}_{\alpha\beta}$  and shear viscosity  $\eta = -\frac{1}{s}\widehat{P}_{xy}$ . Other important properties are the geometric thickness  $H$ , and the volume filling factor  $D(z)$ , useful for connecting the dynamical estimates to photometric observations of rings. The steady-state values of all these quantities are determined by the optical thickness of the system  $\tau$ , the size distribution of particles  $n(R)$ , and by their internal density  $\rho$  and elastic properties  $\varepsilon_n, \varepsilon_t$ .

The extraction of the impact frequency  $\omega_c$  is straightforward both in the instantaneous impact and force method simulations (total number of impact detections/particle/time interval, divided by factor 2 to avoid counting twice the same impact), as long as the tendency for particle sticking is weak (weak to moderate self-gravity not leading to bound aggregates). In the calculation of impact related mean values, like the average of  $\varepsilon_n$  in the case of velocity dependent elasticity, one can weight with  $v_n$  to exclude the contribution of possible sliding motion, if described by small totally elastic rebounds in the instantaneous impact method.

The flow of momentum across the ring consists of a local contribution, related to the momentum carried with the particles during their random motions between successive impacts, and of a nonlocal contribution, arising due to momentum transferred via impacts or via gravitational forces, between particles at different radial distances (Wisdom and Tremaine, 1988). We denote the particle positions by  $\vec{r}$  and their random velocities by  $\vec{c} = \dot{\vec{r}} - \vec{u}$ , with  $\vec{u}$  standing for the mean flow velocity at  $\vec{r}$ . For simplicity, we restrict our attention to the case of a linear shear profile  $\vec{u} = sx\hat{e}_y$ , where  $\hat{e}_y$  denotes the unit vector in tangential direction.

By definition, the components of the pressure tensor  $P_{\alpha\beta}$  give the amount of  $\beta$ -component of momentum transferred in  $\alpha$ -direction, per unit area and unit time. When evaluating the momentum flow in simulations, it is convenient to include all particles and impacts, regardless of their vertical coordinate. This corresponds to a vertical averaging

$$\overline{\widehat{P}_{\alpha\beta}} = \int_{-\infty}^{\infty} \widehat{P}_{\alpha\beta} dz \quad (1.75)$$

From hereon we denote  $\overline{\widehat{P}_{\alpha\beta}}$  simply by  $\widehat{P}_{\alpha\beta}$ , thus having the units of momentum/unit time/unit length.

The local contribution to the pressure tensor is obtained by adding the momenta  $p_\beta = mc_\beta$  of the  $N$  particles, moving with velocity  $c_\alpha$  with respect to the mean flow,

$$P_{\alpha\beta}^{local} = \frac{1}{A_o} \sum_i^N m_i (c_\alpha)_i (c_\beta)_i = \overline{m c_\alpha c_\beta}, \quad (1.76)$$

where  $A_o$  is the area of the simulation region and  $n = N/A_o$  denotes the surface number density. The bar indicates average over particles. Once the steady-state has been achieved,

one can improve the accuracy by averaging over arbitrarily long time intervals.

The standard formula for nonlocal momentum transfer is (Wisdom and Tremaine 1988)

$$P_{\alpha\beta}^{nl} = \frac{1}{A_o \Delta t} \sum_{impacts} m_{>} \Delta r_\alpha \delta c_{\beta>}, \quad (1.77)$$

where the summation is over all impacts occurring during the time interval  $\Delta t$ , and  $m_{>} \delta c_{\beta>}$  denotes the change of the momentum of the particle with the larger  $r_\alpha$  in each impact, and  $\Delta r_\alpha$  the absolute difference in the  $r_\alpha$ -coordinates of the impacting particles. However, application of this formula is problematic in the case of strong particle grouping, as it may be difficult to identify the separate impacts. For the case of force-method impact calculation, the collisional change of momentum is

$$m_{>} \delta c_{\beta>} = \int_{T_{dur}} F_{\beta>} dt, \quad (1.78)$$

where  $F_{\beta>}$  denotes the impact force felt by the particle with the larger  $r_\alpha$  coordinate, and  $T_{dur}$  is the duration of the impact. By defining

$$F_{\beta>} = \sum_i \sum_{(r_\alpha)_j > (r_\alpha)_i}^j F_\beta^{ij}, \quad (1.79)$$

where  $\vec{F}^{ij}$  stands for the impact force exerted by particle  $i$  on the particle  $j$ , with  $\vec{F}^{ij} \neq 0$  for colliding, overlapping pairs, and zero otherwise, the integral (1.78) can be extended to the whole interval  $\Delta t$ , also covering the possibility of particles experiencing multiple simultaneous impacts, or even a permanent sticking of particles. Summing over all particles then gives an equation corresponding to Eq. (1.77),

$$P_{\alpha\beta}^{nl} = \frac{1}{A_o} \left\langle \sum_i \sum_{(r_\alpha)_j > (r_\alpha)_i}^j ((r_\alpha)_j - (r_\alpha)_i) F_\beta^{ij} \right\rangle, \quad (1.80)$$

where the average is taken over an arbitrary time interval. Furthermore, Eq. (1.80) can obviously be generalized to the momentum flow due to long-range forces, e.g in the case of self-gravity,

$$P_{\alpha\beta}^{grav} = \frac{1}{A_o} \left\langle \sum_i \sum_{(r_\alpha)_j > (r_\alpha)_i}^j -G m_i m_j \frac{((r_\alpha)_j - (r_\alpha)_i)((r_\beta)_j - (r_\beta)_i)}{|\vec{r}_j - \vec{r}_i|^3} \right\rangle. \quad (1.81)$$

Likewise,  $\vec{F}^{ij}$  can be identified with adhesive forces, Eq. (1.80) then giving their contribution to the nonlocal pressure. In the case of well defined separate impacts, Eqs. (1.77) and (1.80) give identical results for the nonlocal pressure tensor.

The corresponding contributions to the (vertically integrated) dynamic shear viscosity are readily evaluated from

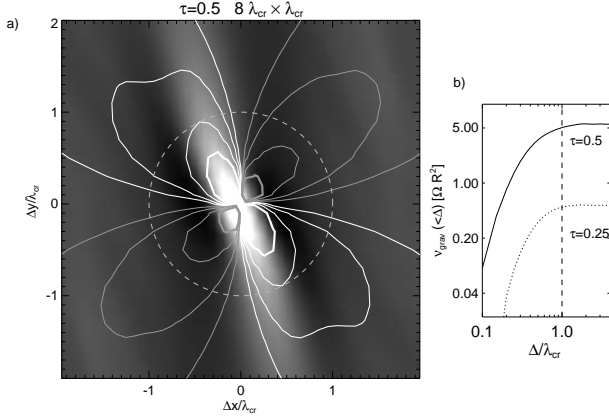


**Figure 1.7** a) The contributions to gravitational viscosity (Eq. 1.85). The contours indicate the mean torque density exerted from relative location  $(\Delta x, \Delta y)$ : positive (white contours) by the particles on the trailing quadrants and negative (gray contours) from the leading quadrants. The gray scale background image is the 2D auto-correlation function (Eq. 1.91) for the same simulation. Note the slightly larger positive net torques arising due to overdensities in the trailing quadrants. In b) the cumulative gravitational viscosity due to material within a circular radius  $\Delta$  is shown as a function of  $\Delta/\lambda_{cr}$ .

$\eta = -\frac{1}{s} P_{12}$ . In the case of Keplerian shear,  $s = -\frac{3}{2}\Omega$ ,

$$\eta_{local} = \frac{2}{3\Omega} n \langle \overline{m c_x c_y} \rangle, \quad (1.82)$$

$$\eta_{nl} = \frac{2}{3\Omega} \frac{1}{A_o \Delta t} \sum_{impacts} m_{>} \Delta x_{>} \langle \delta c_y \rangle, \quad (1.83)$$

$$= \frac{2}{3\Omega} \frac{1}{A_o} \left\langle \sum_i \sum_{\substack{j \\ x_j > x_i}} \Delta x_{>} \langle F^{ij}_y \rangle \right\rangle, \quad (1.84)$$

$$\eta_{grav} = \frac{2}{3\Omega} \frac{1}{A_o} \left\langle \sum_i \sum_{\substack{j \\ x_j > x_i}} -G m_i m_j \frac{(x_j - x_i)(y_j - y_i)}{|\vec{r}_j - \vec{r}_i|^3} \right\rangle. \quad (1.85)$$

The kinematic shear viscosities are obtained from these, dividing by the surface mass density of the system  $\Sigma = n\bar{m}$ . In particular, in the case of identical particles (Wisdom and Tremaine, 1988)

$$\nu_{local} = \frac{2}{3\Omega} \overline{c_x c_y}, \quad (1.86)$$

$$\nu_{nl} = \frac{2}{3\Omega} \frac{1}{N \Delta t} \sum_{impacts} \Delta x_{>} \langle \delta c_y \rangle. \quad (1.87)$$

The above formula for gravitational viscosity is identical to that in Daisaka et al. (2001). Fig. 1.7 shows the contributions to the integrand of Eq. 1.85, arising from different relative locations  $\Delta x = x' - x$ ,  $\Delta y = y' - y$ . Largest gravitational torques are exerted by material within  $\sim 0.25\lambda_{cr}$ , and almost all of  $\nu_{grav}$  is due to particles within one  $\lambda_{cr}$ .

The velocity dispersion tensor is collected by sampling the random velocity components of each particle with short intervals and tabulating the averages values as function of simulation time. In particular, in Sect. 1.8 we will use the time-averaged 1-d velocity dispersion  $c$  to characterize the

dynamical 'temperature' of the system

$$c^2 = \frac{1}{3} \left\langle \overline{c_x^2 + c_y^2 + c_z^2} \right\rangle = \frac{1}{3} \frac{tr \hat{P}^{local}}{\Sigma} \quad (1.88)$$

The vertical thickness is defined as

$$H = \sqrt{12z^2}, \quad (1.89)$$

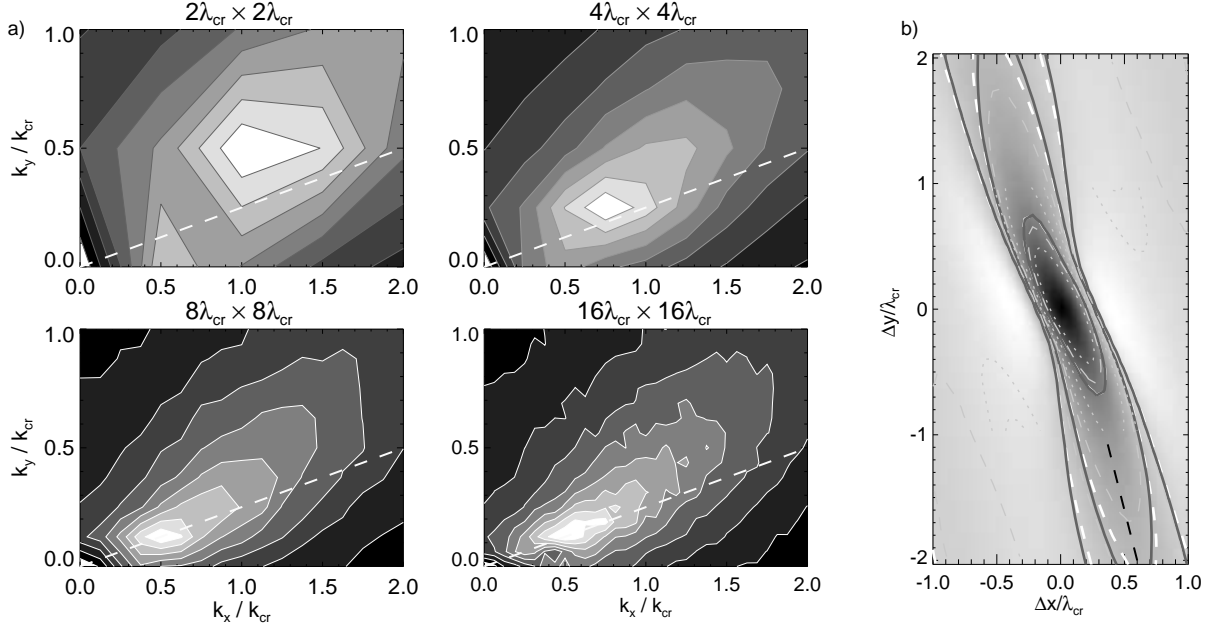
which corresponds to the full thickness of a uniform layer with the same vertical dispersion as the simulated particle field. The vertical distribution can be further characterized by tabulating the vertical density profile of the simulation particles. This can be based on the locations of particle centers (Wisdom and Tremaine, 1988), or by  $D(z)$  indicating the fraction of volume filled by particles as a function of  $z$  (Salo and Karjalainen, 2003). In particular, the filling factor at the equatorial plane  $D(z=0)$  (often denoted as  $FF(0)$ ) is useful in comparison to theoretical treatments of dense rings (Araki and Tremaine, 1986; Araki, 1991).

Other hydrodynamic quantities besides  $\nu$  can also be extracted from simulations, like the radial heat conductivity and bulk viscosity, and the temperature derivatives of pressure, shear viscosity and energy dissipation. Such tabulations were made in Salo et al. (2001) for systems with various values of  $\Omega_z/\Omega$ . However, compared to the shear viscosity that can be extracted at the steady-state, these other quantities require that the system is perturbed and the measurement is carried out while the system relaxes back toward the uniform steady-state. Besides the technical difficulties involved, the exact relation of the derived quantities to their hydrodynamic interpretation is not clear. Mainly this is due to the non-isotropic velocity distribution (see Fig. ??e) following from particle's orbital motion around the planet. Such a distribution has more degrees of freedom than taken into account in hydrodynamical treatment. Nevertheless, such 'fitted' quantities applied to hydrodynamic stability analysis are quite successful in describing the viscous stability properties of larger-scale simulations (Schmidt et al., 2001; Schmidt and Salo, 2003).<sup>2</sup>

### 1.5.2 Characterization of self-gravity wakes

Examples of self-gravitating simulations were shown in Fig. 1.5 comparing snapshots from simulations with different sized calculation regions, while keeping other parameters the same. The snapshots indicated that the typical appearance of wake structure is evident even for calculation regions as small as  $2\lambda_{cr} \times 2\lambda_{cr}$ . However, comparison of gravitational viscosity (see Sect. 1.5) indicates that the strength of wakes is not fully developed unless a few times larger region, say  $8\lambda_{cr} \times 8\lambda_{cr}$  is simulated. Similarly, the spacing and pitch angle of wakes is affected by the periodic boundaries: this is illustrated in Fig. 1.8a in terms of 2D Fourier decomposition

<sup>2</sup> Isothermal hydrodynamical models which ignore bulk viscosity and temperature derivatives (Schmit and Tscharnuter, 1995) give qualitatively correct picture of viscous behavior but fail to predict quantitatively the correct regimes of viscous instability and overstability.



of surface density

$$\Sigma(x, y) = \Sigma_0 \sum_{l, m} \tilde{\Sigma}_{l, m} \exp\left(i \frac{2\pi l}{L_x} x + i \frac{2\pi m}{L_y} y\right) \quad (1.90)$$

where  $|\tilde{\Sigma}_{l, m}|$  gives the normalized amplitude corresponding to the radial and tangential wavelengths  $\lambda_x = L_x/l$  and  $\lambda_y = L_y/m$ .<sup>3</sup> In the  $2\lambda_{cr} \times 2\lambda_{cr}$  simulation the peak amplitude occurs at  $(\lambda_x, \lambda_y) = (1, 2)\lambda_{cr}$ , but when the region is increased,  $(\lambda_x, \lambda_y)$  approaches  $(2, 8)\lambda_{cr}$ . This corresponds to a pitch angle  $\tan^{-1}(\lambda_x/\lambda_y) \approx 14^\circ$  between tangential direction and the the average direction of wakes.

The shape and orientation of the wakes is best illustrated in terms of 2D auto-correlation function of surface density,

$$\zeta_{2d}(\Delta x, \Delta y) = \frac{1}{\Sigma_0^2 A_0} \int \int \Sigma(x + \Delta x, y + \Delta y) \Sigma(x, y) dx dy \quad (1.91)$$

Taking the time average of this describes the typical density structure the particle sees around its location. It can be calculated directly from stored particle snapshots (e.g. Salo 1995), or more conveniently (e.g. Toomre and Kalnajs 1991) with the FFT, by taking the inverse Fourier transform of the squared density amplitudes,  $\zeta_{2d} = |\tilde{\Sigma}_{l, m}|^2$ . Figure 1.8b displays the auto-correlation functions, together with a line corresponding to  $14^\circ$  pitch angle.

### 1.5.3 Energy budget in local simulations

In the steady-state, the energy dissipation rate is connected to momentum flow by

$$\dot{E}_{diss} - sP_{12} = 0 \quad (1.92)$$

<sup>3</sup> A convenient way to calculate the amplitudes is to perform 2D FFT on the system whenever the image regions happen to be aligned along the x-axis, which takes place  $3\pi L_x/L_y$  times per orbit; at these instants FFT can be readily applied as  $\Sigma$  is periodic in both x and y.

**Figure 1.8** a) Fourier amplitudes  $|\tilde{\Sigma}_{l, m}|$  (see Eq. 1.90) in the simulations of Fig. 1.5, as a function of wavenumbers  $k_x = 2\pi/\lambda_x$  and  $k_y = 2\pi/\lambda_y$ , where  $\lambda_x$  and  $\lambda_y$  are the radial and tangential wavelengths. The contours indicate amplitude levels 0.1,...0.9 times the maximum amplitude. The dashed line indicates  $k_y = 0.25k_x$ , corresponding to a pitch angle  $\approx 14^\circ$ . In b) time averaged 2D auto-correlation functions of the same simulations (Eq. 1.91). Solid black and dashed white contours correspond to  $16\lambda_{cr} \times 16\lambda_{cr}$  and  $8\lambda_{cr} \times 8\lambda_{cr}$  simulations. Dashed black line indicates a  $14^\circ$  asymptotic pitch angle.

where  $\dot{E}_{diss}$  is the energy loss in impacts, per unit time and unit area. Although this formula is valid for any shear flow, it is instructive to check how the formula actually arises in a local calculation region with periodic boundaries.

As mentioned in section 1.2, the quantity (Eq. 1.11)

$$E = E_{kin} + E_{pot} + E_{grav} \quad (1.93)$$

with

$$E_{kin} = \sum_i \frac{1}{2} m_i (\dot{x}_i^2 + \dot{y}_i^2 + \dot{z}_i^2) \quad (1.94)$$

$$E_{pot} = \sum_i m_i (\Omega s x_i^2 + \frac{1}{2} \Omega_z^2 z_i^2) \quad (1.95)$$

$$E_{grav} = -\frac{1}{2} G \sum_i \sum_{j \neq i} \frac{m_i m_j}{|\vec{r}_j - \vec{r}_i|} \quad (1.96)$$

is conserved along the orbital motion of particles. On the other hand,  $E$  changes both due crossing of radial boundaries and due impacts, via changes in  $E_{kin}$ , while both  $E_{pot}$  and  $E_{grav}$  remain unchanged<sup>4</sup>.

The above expression for  $E_{kin}$ , using the actual velocities of the simulation particles, includes both, the kinetic energy

<sup>4</sup> Assuming that gravitational forces are constructed using the nearest image pairs, in which case the distances  $|\vec{r}_i - \vec{r}_j|$ 's are not affected.

associated to their random motions,  $E_{rnd}$ , and the kinetic energy associated to the systematic shear flow  $E_{shear}$ ,

$$E_{kin} = E_{rnd} + E_{shear} \quad (1.97)$$

where

$$E_{rnd} = \frac{1}{2} \sum_i m_i \bar{c}_i^2 = \sum_i \frac{1}{2} m_i [\dot{x}_i^2 + (\dot{y}_i - s x_i)^2 + \dot{z}_i^2], \quad (1.98)$$

$$E_{shear} = \frac{1}{2} \sum_i m_i [2s x_i (c_y)_i + s^2 x_i^2] \quad (1.99)$$

Since  $E_{rnd}$ , rather than  $E_{kin}$  is of interest in many applications, we next look how it evolves in local simulations, subject to periodic boundaries, collisions, and gravitational forces.

In crossing of boundaries, the random velocity relative to mean flow is unaffected, so that  $\Delta E_{rnd}$  remains constant, the change of  $E_{kin}$  being associated solely with  $E_{shear}$ . In an impact of a particle pair

$$\begin{aligned} \frac{1}{2} \delta(m_1 \bar{v}_1^2 + m_2 \bar{v}_2^2) &= \frac{1}{2} \delta(m_1 \bar{c}_1^2 + m_2 \bar{c}_2^2) \\ &+ s [m_1 x_1 (\delta c_y)_1 + m_2 x_2 (\delta c_y)_2], \end{aligned} \quad (1.100)$$

where the last term can be combined to  $s m_2 (\delta c_y)_2 (x_2 - x_1)$ , using the conservation of momentum ( $\varrho$  labels the particle with larger radial coordinate). Summing over all impacts during the time interval  $\Delta t$  we have

$$(\Delta E_{rnd})^{coll} = \Delta E_{diss} - s \sum_{impacts} m_{>} (\delta c_y)_{>} \Delta x_{>}. \quad (1.101)$$

To obtain the change of  $E_{rnd}$  due to self-gravity and orbital motion, we use Eqs. (1.93) and (1.97) to write

$$\begin{aligned} E_{rnd} &= E - E_{grav} - E_{pot} - E_{shear} \\ &= E - E_{grav} - E_z \\ &- \sum_i m_i \left[ (\Omega s + \frac{1}{2} s^2) x_i^2 + s x_i (\dot{y}_i - s x_i) \right] \end{aligned} \quad (1.102)$$

where

$$E_z = \frac{1}{2} \sum_i m_i \Omega_z^2 z_i^2 \quad (1.103)$$

denotes the potential energy associated with vertical motions. Since  $E$  is conserved during orbital motion, the change of  $E_{rnd}$  during time interval  $\Delta t$  equals

$$\begin{aligned} (\Delta E_{rnd})^{orb} &= -\Delta(E_{grav} + E_z) \\ &- \int_t^{t+\Delta t} \sum_i m_i \left[ (2\Omega s + s^2) x_i \dot{x}_i \right. \\ &\left. + s \dot{x}_i (\dot{y}_i - s x_i) + s x_i (\ddot{y}_i - s \dot{x}_i) \right] dt. \end{aligned} \quad (1.104)$$

Substituting  $\ddot{y} = -2\Omega \dot{x} + (F_y)_i/m_i$  from the equation of motion, where  $(F_y)_i/m_i$  is the y-component of the gravitational force felt by particle  $i$ , and taking into account that  $c_x = \dot{x}$ ,

$$\begin{aligned} (\Delta E_{rnd})^{orb} &= -\Delta(E_{grav} + E_z) \\ &- s \Delta t \left\langle \sum_i m_i (c_x)_i (c_y)_i + \sum_i x_i (F_y)_i \right\rangle \end{aligned} \quad (1.105)$$

Adding  $(\Delta E_{rnd})^{coll}$  and  $(\Delta E_{rnd})^{orb}$ ,

$$\begin{aligned} \Delta E_{rnd} &= \Delta E_{diss} - \Delta(E_{grav} + E_z) - s \sum_{impacts} m_{>} (\delta c_y)_{>} \Delta x_{>} \\ &- s \Delta t \left\langle \sum_i m_i (c_x)_i (c_y)_i \right\rangle - s \Delta t \left\langle \sum_i x_i (F_y)_i \right\rangle \end{aligned} \quad (1.106)$$

Clearly, the summation in the last term in the right-hand size can be arranged to a form involved in the formula for gravitational viscosity Eq. (1.85). Dividing by  $\Delta t$  and  $A_o$  thus gives

$$\dot{E}_{rnd} + \dot{E}_{grav} + \dot{E}_z = \dot{E}_{diss} - s P_{xy} = \dot{E}_{diss} + s^2 \eta \quad (1.107)$$

where the total viscous gain  $-s P_{xy}$  consists of local, nonlocal and gravitational viscosity contributions

$$P_{xy} = P_{xy}^{local} + P_{xy}^{nl} + P_{xy}^{grav} \quad (1.108)$$

In the steady-state the left hand side of Eq. (1.107) is zero, leading to the anticipated result in Eq. 1.92.

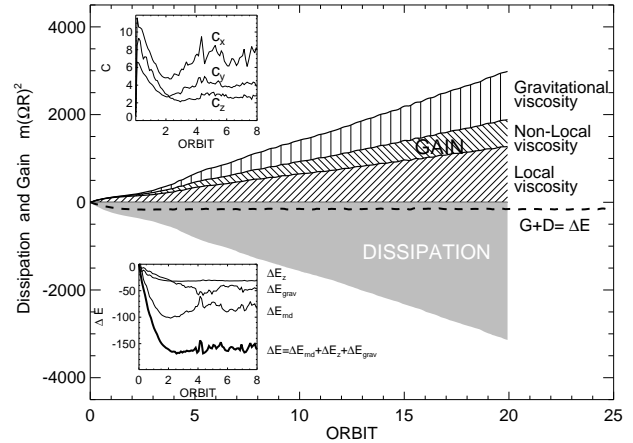


**Figure 1.9** Energy balance in the  $4\lambda_{cr} \times 4\lambda_{cr}$  simulation of Fig 1.5. Different contributions to viscous gain are shown separately: in the steady-state they balance the collisional dissipation. The small difference in the cumulative sum of gain and dissipation (G+D, dashed curve) equals the change in the total energy ( $\Delta E = \Delta E_{rnd} + \Delta E_{grav} + \Delta E_z$ ) when the system settled toward steady-state values from an initially 'hot' state: the upper insert shows the random velocity components, and the lower insert the various components of energy change. The energies are shown in units of  $m(R\Omega)^2$ , where  $m$  is the total mass of simulation particles.

An example of energy balance in simulations is shown in Fig. 1.9 for a system that starts with a velocity dispersion exceeding the steady-state value. Initially both  $\dot{E}_{rnd}$  and  $\dot{E}_z$  are negative as the system cools and flattens down toward steady-state. Also the negative contribution of gravitational energy increases when the particles collect to dense wakes. In steady-state, the left-hand size of Eq. (1.107) vanishes and the rates of viscous gain and dissipation balance each other exactly.

## 1.6 Advanced computational techniques (Mark)

pair search

- parallelization
- treatment of aggregates
- streamline simulations
- Rein - Rebound
- Hahn -streamline method
- Grape-simulations

## 1.7 Three-body/Embedded moonlets (Keiji, Mark, Heikki)

## 1.8 Survey of simulation results

This Section collects simulation examples illustrating the intrinsic local dynamics of planetary ring systems. We start by discussing the simplest case of identical, non-selfgravitating particles, and demonstrate how the characteristics of the system's steady-state, e.g. the frequency of impacts and the velocity dispersion, depend on the coefficient of restitution and particle size. We show that the simulation results are consistent with heuristic hydrodynamical estimates. Particles' spin rotation, induced by surface friction and irregularities, is also briefly examined. We then proceed to systems with a distribution of particle sizes, and finally also include the particles' mutual self-gravity,

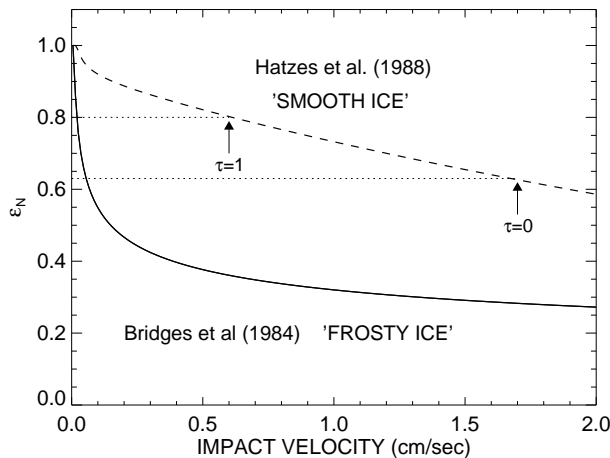


**Figure 1.10** Two velocity-dependent elasticity models describing laboratory measurements of icy particles. The curve labeled 'frosty' is for frost-covered ice (Bridges et al., 1984),  $\varepsilon_n(v_n) = 0.32(v_n)^{-0.234} < 1$ , while the curve 'smooth' refers to particles with compacted-frost surfaces (Hatzes et al., 1988),  $\varepsilon_n(v_n) = 0.90e^{-0.22v_n} + 0.01v_n^{-0.6}$ . The normal component of impact velocity  $v_n$  is expressed in cm/sec. Note that the measurements had a large scatter around the fits.

Our main goal is to understand how the dynamic viscosity varies with surface density, and how this relation depends on particles' physical properties. As mentioned above, this

$\eta(\Sigma)$  relation is crucial for the large-scale viscous stability properties of the particle ensemble. For non-gravitating systems the surface density is replaced with optical depth and dynamic viscosity then corresponds to  $\eta = \nu\tau$ . Two models (Fig 1.10) for velocity-dependent coefficient of restitution are systematically compared, corresponding to laboratory measurements made by Bridges et al. (1984; 'frosty' ice) and Hatzes et al. (1988; 'smooth' ice). The former model, with a steeper drop of  $\varepsilon_n$  with impact velocity leads to an energy balance where the velocity dispersion corresponds to ring vertical thickness  $H \sim 10$  meters, (when assuming 1 meter ring particles), while the latter model implies a much hotter multilayer ring with  $H \sim 100$  meters: these two models serve to illustrate the uncertainty in ring particles' elastic properties. The viscosity versus density relation is constructed from small-scale simulations whose radial size is smaller than the shortest unstable wavelength so that no viscous perturbations can grow. It turns out that the two models predict drastically different viscous behavior: viscous instability in the case of thick rings and overstability in the case of flattened rings. Indeed, when the size of the simulation system is made sufficiently large both viscous instabilities and overstabilities can be directly verified in simulations (see Sect 1.9).

### 1.8.1 Simulations of non-selfgravitating systems

#### 1.8.1.1 Impact frequency

The ring system rapidly establishes an energy balance where the collisional dissipation is compensated by the viscous transfer of energy from the systematic orbital motion to random motions (Sect. 1.5.3). The time scale to reach this steady-state is determined by the frequency of particles' mutual impacts,  $\omega_c$ . As expected, the impact frequency increases proportional to optical depth  $\tau$ . An important peculiarity of planetary ring dynamics is that the steady-state  $\omega_c$  is practically independent from the velocity dispersion. This results from the partitioning of vertical and horizontal random motions via impacts. Thus for example an increase in velocity dispersion, which in itself would enhance  $\omega_c$ , is compensated by a corresponding vertical thickening and thereby reduced space density.<sup>5</sup> Analytical treatments taking into account the anisotropic distribution of impact directions and a Gaussian vertical profile (e.g. Hameen-Anttila 1978), indicate

$$\omega_c \sim 3\tau\Omega \sim 20\tau \text{ impacts/orbit}, \quad (1.109)$$

The independence of  $\omega_c$  on velocity dispersion is illustrated in Fig. 1.11a, together with the approximation of Eq. 1.109 (dashed line). For comparison, the figure also shows  $\omega_c$  in a 2D simulation where the motion of particles is limited to the

<sup>5</sup> The basic formula is  $\omega_c \propto n_s c \sigma_c$ , where  $n_s$  is the space number density,  $c$  is the 1-dimensional velocity dispersion and  $\sigma_c$  the collisional cross-section:  $\sigma_c = 4\pi R^2$  assuming identical particles with radius  $R$ . The space density  $n_s \approx n/H$ , where  $n = \tau/(\pi R^2)$  is the surface number density and  $H$  the vertical thickness. Due to collisional coupling of horizontal and vertical motions,  $c_z \sim c$ , while due to orbital motion  $H \propto c_z/\Omega$ . The explicit  $n_s$  and  $c$  dependencies thus cancel out, leading to formula 1.109,

central plane. In this case no adjustment between velocity dispersion and space density is possible and the explicit velocity dispersion dependence in  $\omega_c$  is retained. As discussed in Salo and Schmidt (2011) this leads to fundamental differences in the viscosity versus density relations and thus the stability properties of 2D and 3D simulation systems.

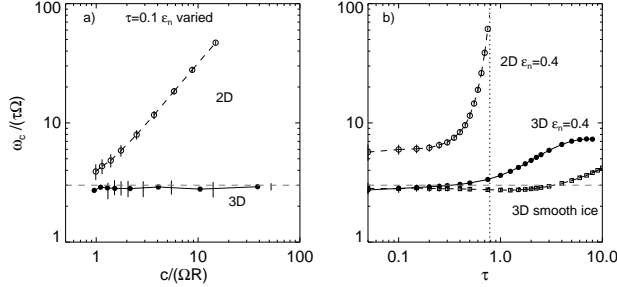


**Figure 1.11** Impact frequency  $\omega_c$  in 3D and 2D simulations, normalized to  $\Omega\tau$ . In a) simulations with fixed  $\tau = 0.1$  are compared as a function of velocity dispersion  $c$ , normalized to  $R\Omega$ ; the points correspond to steady-state values in simulations with different coefficient of restitution. In b)  $\omega_c$  as a function of optical depth for simulations with constant  $\epsilon_n = 0.4$  (circles) and using the Hatzes et al. (1988) velocity-dependent  $\epsilon_n$  (see Fig. 1.10). The vertical line indicates the  $\tau_{max}$  for 2D systems.

The linear dependence of  $\omega_c$  on  $\tau$  breaks down for flattened systems ( $H/R \sim 1$ ) when  $\tau \gtrsim 1$ , in which case the particles' own volume limits the free space available for motion (Hämeen-Anttila 1978). Similarly in a 2D system the impact frequency increases dramatically when the maximum 2D packing limit ( $\tau_{max} = \pi/4 \approx 0.785$  for identical particles) is approached. On the other hand, for a hot 3D multilayer ring ( $H/R \gg 1$ ) the simple approximation holds quite well even for  $\tau > 1$ .

### 1.8.1.2 Establishment of Local Energy balance

Figure 1.12 displays the time evolution of the velocity dispersion  $c$  in simulations with different elasticity models. For a constant  $\epsilon_n$  sufficiently close to unity  $c$  increases exponentially with time, and clearly no steady-state is achieved. A constant  $\epsilon_n$  closer to zero leads to an exponential drop until  $c$  levels at a few times  $R\Omega$ , corresponding to a few particle diameter thick ring. On the other hand, in the case of  $\epsilon_n(v_n)$  the steady-state depends on the functional form of the relation. The Bridges et al. (1984) model ('frosty' ice) leads to a flattened system very similar to  $\epsilon_n \approx 0.5$ , whereas the Hatzes et al. (1988) model ('smooth' ice) leads to a multilayer ring. Fig 1.12b also illustrates the rapid time scale of evolution: here the system forgets the initial conditions in roughly 50 orbital periods, which for the used  $\tau = 0.1$  corresponds to about 100 impacts/particle.

The above velocity evolution can be qualitatively explained with a simple heuristic description of the energy balance between dissipation and viscous gain (see Stewart et al (1984), Schmidt et al. (2009)). According to Eq. (1.107),

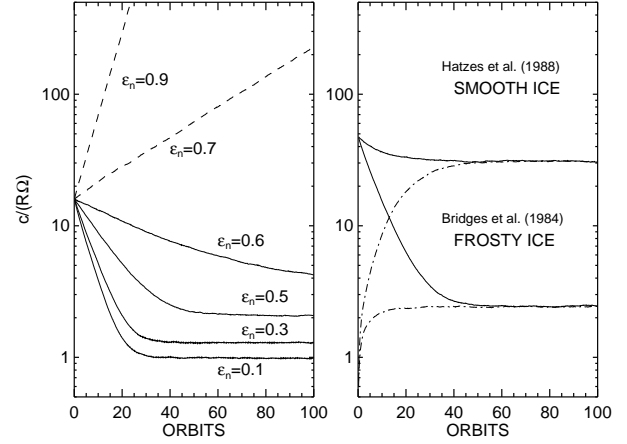


**Figure 1.12** a) Evolution of velocity dispersion in simulations with different value of constant coefficient of restitution  $\epsilon_n$ , for optical depth  $\tau = 0.1$ . The critical value  $\epsilon_n \approx 0.65$  separates the thermally stable (solid) and unstable (dashed) systems. (b) Simulations with two velocity dependent elasticity models of Fig. 1.10, starting from different initial states. Now the system attains a steady-state with the final velocity dispersion depending on the  $\epsilon_n(v_n)$  relation: the 'smooth' ice model with a shallower drop of elasticity with  $v_n$  leads to a much hotter steady-state than the 'frosty' ice model where  $\epsilon_n$  drops very fast with  $v_n$ .

the rate of kinetic energy change/unit mass is

$$\dot{E}_{rnd}/\Sigma + \dot{E}_z/\Sigma = \dot{E}_{diss}/\Sigma + s^2\nu \quad (1.110)$$

Inserting the Keplerian shear rate  $s = -\frac{3}{2}\Omega$  and averaging the energy dissipation in individual impacts (Eq. 1.43; keeping just the  $\epsilon_n$  contribution, and absorbing the term  $\dot{E}_z$  which relates to vertical flattening into  $\dot{E}_{rnd}$ ), we can write

$$\frac{1}{2}dc^2/dt = -k_1\omega_c c^2(1 - \epsilon_n^2) + \frac{9}{4}\Omega^2 \left[ \underbrace{k_2 c^2 \frac{\omega_c}{\omega_c^2 + \Omega^2}}_{\nu_{local}} + \underbrace{k_3 \omega_c R^2}_{\nu_{nl}} \right], \quad (1.111)$$

where the viscosity has been written as a sum of local and nonlocal contributions, and  $k_1, k_2, k_3$  are all constants of the order of unity. The basic expression for local viscosity is  $\nu_{local} = \omega_c \lambda^2$ , where  $\lambda$  is the radial mean free path between impacts. In the high impact frequency regime the impacts limit the mean free path to  $\lambda \sim c/\omega_c$  while for low  $\omega_c$  an upper bound is set by the amplitude of epicyclic excursions,  $\lambda \sim c/\Omega$ . Combining these estimates (Goldreich and Tremaine, 1978) leads to the form in Eq. (1.111). For the non-local term the  $\lambda$  is set equal to the particle radius  $R$ .

The Eq. (1.111) describes qualitatively quite well the simulated behavior for a given elasticity of particles. In particular, if the system is very hot,  $c/(R\Omega) \gg 1$ , the nonlocal gain term can be ignored. In this case both the gain and dissipation terms in the right hand side are proportional to  $c^2$ . Thus, no balance is possible unless  $\epsilon_n$  equals a critical value  $\epsilon_{cr}$ , which (approximating  $\omega_c \sim \Omega\tau$ ) depends on the optical

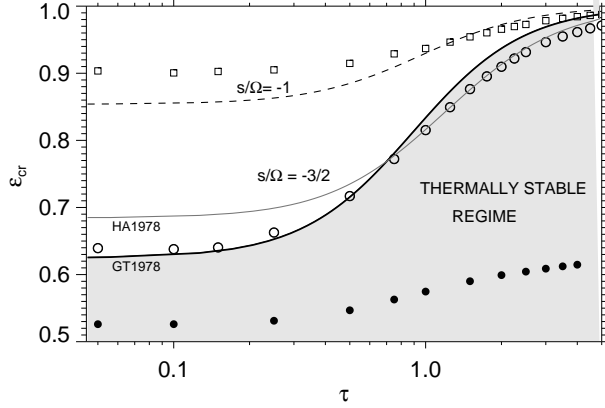


**Figure 1.13** Thick solid line is the Goldreich-Tremaine  $\varepsilon_{\text{cr}}(\tau)$  relation; thin solid line is the  $\varepsilon_{\text{cr}}$  from Hmeen-Anttila (1978). Systems with constant  $\varepsilon_n < \varepsilon_{\text{cr}}(\tau)$  (shaded region) flatten toward a stable near-monolayer state, while those with  $\varepsilon_n > \varepsilon_{\text{cr}}(\tau)$  disperse via growing random velocities. Dashed line shows an approximate critical curve for a flat velocity field with  $s/\Omega = -1$  (obtained by replacing  $9/4$  with  $1$  in 1.112). Open symbols indicate effective mean values of  $\varepsilon_n$  in dynamically hot simulations with  $c/(\Omega R) \gg 1$  (Bridges-type velocity-dependent elasticity formula, but with 100-fold velocity scale factor). For comparison, solid symbols indicate effective  $\varepsilon_n$  in simulations with the original Bridges elasticity law. Note that the effective mean of  $\varepsilon_n$  depends on how impacts are weighted (Salo, 1987b); here we use  $\varepsilon_{\text{eff}} = \langle \varepsilon_n(v_n)v_n^2 \rangle / \langle v_n^2 \rangle$ .

depth via the well-known Goldreich-Tremaine formula

$$(1 - \varepsilon_{\text{cr}}^2)(1 + \tau^2) = \frac{9k_2}{4k_1} \approx 0.61. \quad (1.112)$$

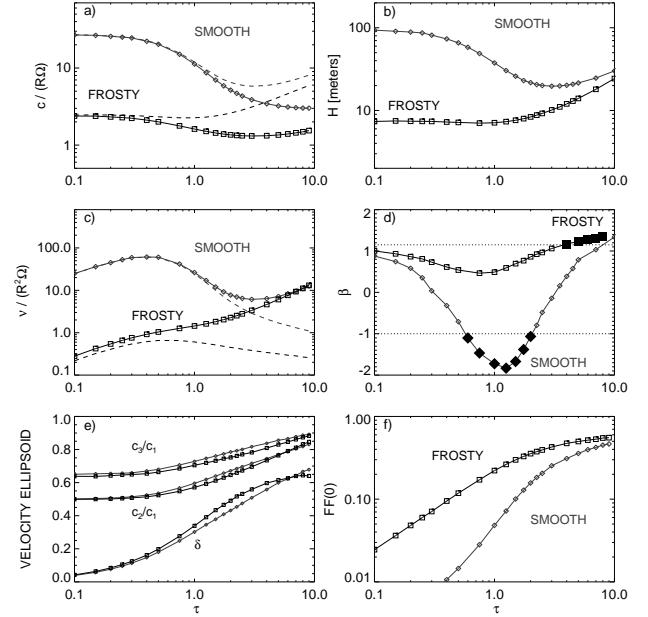
If the constant  $\varepsilon_n > \varepsilon_{\text{cr}}$ , velocity dispersion increases continuously, as the dissipation is too weak to balance the local viscous gain. Similarly, if the constant  $\varepsilon_n < \varepsilon_{\text{cr}}$ , then dissipation exceeds the local viscous gain, leading to reduced  $c$ . The eventual steady-state is determined by the nonlocal gain implying a final  $c \propto \Omega R$ . According to Eq. (1.112),  $\varepsilon_{\text{cr}} \approx 0.65$  for  $\tau \rightarrow 0$ , in good agreement with the low  $\tau$  simulations of Fig. 1.12. In the case of velocity dependent  $\varepsilon_n$ , the behavior is different, since the effective value of  $\varepsilon_n$  depends on the average impact velocity  $\sim c$ . In the limit  $v_{\text{local}} \gg v_{\text{nl}}$  (equivalent to  $c \gg R\Omega$ ), the steady state  $c$  would be adjusted to a value that yields  $\varepsilon_{\text{eff}} = \varepsilon_{\text{cr}}$ , where  $\varepsilon_{\text{eff}}$  is the weighted mean of  $\varepsilon_n(v_n)$  in impacts.

Figure 1.13 shows the Goldreich-Tremaine  $\varepsilon_{\text{cr}}$  as a function of  $\tau$ , delineating the thermally stable ( $\varepsilon_n < \varepsilon_{\text{cr}}$ ) and unstable ( $\varepsilon_n > \varepsilon_{\text{cr}}$ ) regimes. When  $\tau$  is increased, less and less dissipation is allowed for a thermally stable state to exist, so that  $\varepsilon_{\text{cr}}$  approaches unity. This follows from the reduction of local contribution to viscous gain, due to reduced mean free path  $\lambda$  as  $\tau$  increases. Similarly, in the case of a reduced central shear rate, the  $\varepsilon_{\text{cr}}$  would rise toward unity in order to compensate for the less effective viscous gain (for example  $\varepsilon_{\text{cr}} \approx 0.85$  at  $\tau \rightarrow 0$  for a flat rotation curve with  $s = -\Omega$ ).

Also shown in the Fig. 1.13 are the mean values of  $\varepsilon_n$  measured from simulations. Open symbols show simulations which lead to a dynamically hot steady-state with  $c \gg R\Omega$ ,

thus mimicking the conditions leading to Eq. (1.112). In this case the agreement with theoretical approximation is quite obvious. For comparison, filled circles show mean  $\varepsilon_n$  in simulations which lead to a steady-state with  $c/(R\Omega)$  not far from unity: in this case both local and nonlocal viscous gains are important, and the steady-state dissipation rate is larger (mean  $\varepsilon_n$  closer to zero) than implied by the Goldreich-Tremaine formula which takes into account only the local viscous gain.

### 1.8.1.3 Steady-state as a function of optical depth



**Figure 1.14** Steady-state quantities as a function of  $\tau$  in simulations with velocity-dependent coefficient of restitution: in a) the velocity dispersion  $c$  (dashed lines include also the contribution from nonlocal pressure, obtained by using  $\hat{P}^{nl}$  in Eq. (1.88)), in b) the vertical thickness  $H$ , in c) the kinematic viscosity (dashed lines indicate the local contribution), and in d) the slope of  $\nu \propto \tau^\beta$  relation; the values of  $\beta < -1$  predict viscous instability and  $\beta \gtrsim 1$  viscous overstability (large filled symbols), e) shows the axial ratios of the velocity ellipsoid  $c_2/c_1$  and  $c_3/c_1$ , and the angle  $\delta$  between the radial direction and the largest principal axis component, and f) the central plane volume filling factor  $FF(0)$ .

Figure 1.14 collects the various steady state properties as a function  $\tau$ , for the above two  $\varepsilon_n(v_n)$  models. As mentioned earlier, the main difference between the models is the about 10-fold larger velocity dispersion (a) for the smooth ice model at the low  $\tau$  regime. This follows from the shallower slope in the  $\varepsilon_n(v_n)$  relation, indicating that on the average must faster impacts are needed to yield the required dissipation rate. When optical depth increases, there is a strong drop in the  $c$ : this results from the above mentioned reduced local viscous gain: energy dissipation rate adjust by reducing the average impact velocities. For the ‘frosty ice’

model there is hardly any change of  $c$  with  $\tau$ : this is because the local gain term dominates for all  $\tau$ 's. For the 'smooth ice' model the large drop in  $c$  reflects also in the strong flattening of the system (b) and the drop of local kinematic viscosity (c).

The resulting viscosity versus density relations is quantified in Fig. 1.14d where the slope  $\beta = d \log \nu / d \log \tau$  is displayed. Values of  $\beta < -1$  correspond to negative  $d\eta/d\tau$ , the condition for *viscous instability* (collision-induced momentum flux tends to enhance density fluctuations; see Fig. 1.25 for a schematic illustration). In principle  $\beta > -1$  indicates viscous stability (collisions smooth density fluctuations). However, particle simulations (Salo et al. 2001) and hydrodynamical models (Schmidt et al 2001) indicate that for  $\beta > 1$  the system may be prone to *viscous overstability*. The 'smooth ice' elasticity model implies instability for  $0.7 \lesssim \tau \lesssim 2$ , while the 'frosty ice' fulfills condition for overstability if  $\tau \gtrsim 4$ . We check these predictions in Section 1.9 with radially more extended simulations.

The lowermost row in Fig. 1.14 shows the shape and orientation of the velocity ellipsoid. Regardless of the large difference in the steady-state velocity dispersion, the principal axial ratios are not very different for the two models. At the limit  $\tau \rightarrow 0$  the ratio  $c_2/c_1 \rightarrow 0.5$  for both models, being determined solely by the systematic gradient in the Keplerian velocity field. On the other hand, the ratio  $c_3/c_1$  depends somewhat on the effectivity of collisions in transferring energy from horizontal to vertical motions: this ratio is smaller in the case of more inelastic models yielding flatter systems. With increased  $\tau$ , both  $c_2/c_1$  and  $c_3/c_1$  increase toward unity, though even at the largest studied value,  $\tau = 10$ , the velocity ellipsoid is still far from isotropic, even if the impact frequency already corresponds to over 100 impacts/orbital period. Likewise, the deviation  $\delta$  of the longest principal axis from the radial direction, increases with  $\tau$ , but is still considerably below the hydrodynamical limit  $\pi/4$  even at  $\tau = 10$ . Also shown is the central plane volume filling factor of the two models: for the 'frosty' ice model,  $FF(0)$  exceeds 0.2 for  $\tau > 1$ , while for the 'smooth ice' model the same requires  $\tau > 3$ . Comparison to Fig. 1.11 indicates that this is roughly the regime where the nonlinearity of  $\omega_c$  versus  $\tau$  becomes apparent.

The above simulation survey for 'frosty' and 'smooth' elasticity models was done using 1 meter particles at the distance of 100 000 km. In this case the 'smooth ice' model was dominated by local viscosity at low  $\tau$ , while with the 'frosty' ice model local viscosity dominated at all  $\tau$ 's. Consequently, the former model is susceptible for viscous instability while the latter model is not. To remind that this behavior depends on the assumed particle size/elasticity model combination, Fig 1.15 compares the expected behavior of the 'frosty ice' model when using particles sizes of 0.01, 0.10 and 1 meters. For a rough estimate of the relative importance of local and nonlocal contributions, note that at  $\tau \rightarrow 0$  the local contribution tries to establish a state with a mean  $\varepsilon_n \approx 0.65$ . For the Bridges et al. (1984) frosty ice model this corresponds to  $c_{\text{local}} \approx 0.05$  cm/s. On the other hand, the nonlocal contribution maintains a minimum  $c_{\text{nonlocal}} \approx R\Omega = 0.2$  cm/sec with the nominal values

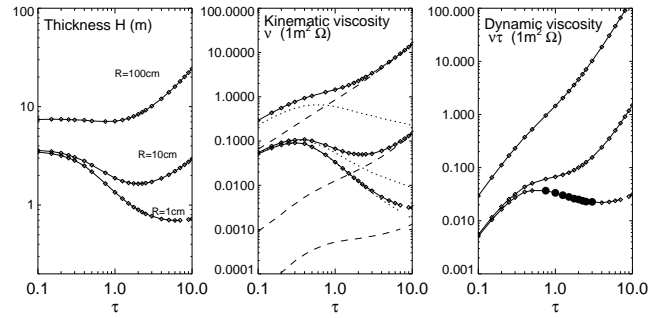


**Figure 1.15** Dependence of a) geometric thickness  $H$ , b) kinematic viscosity  $\nu$ , and c) dynamic viscosity  $\eta = \nu\tau$  on optical depth  $\tau$ , for the 'frosty' ice model of the previous figure, but with different sized simulation particles. Large solid circles in c) indicate viscously unstable regime. In b) dotted and dashed lines indicate separately the local and nonlocal contributions.

of the previous figures. Thus with 1 meter particles  $c_{\text{nonlocal}}$  exceeds  $c_{\text{local}}$  by a factor of 4. However, with 1 cm simulation particles,  $c_{\text{nonlocal}} \ll c_{\text{local}}$ , and a strong drop in the steady-state  $c$  around  $\tau \sim 1$  is again present. This would again lead to viscously unstable behavior for intermediate  $\tau$ 's.

#### 1.8.1.4 Surface friction and Particle spins

In contrast to the normal coefficient of restitution, relatively few measurements exist for the friction of icy particles. According to Supulver et al. (1995) experiments, friction is weak, corresponding to tangential coefficient of restitution  $\varepsilon_t \sim 0.9$  in the case of relatively smooth ice surfaces at temperatures near 100 K. Nevertheless, to illustrate the possible effects of tangential friction we will briefly examine the whole allowable range of  $1 \geq \varepsilon_t \geq -1$ , the latter extreme corresponding to the case where friction is able to reverse the tangential relative velocity in impact. Also, as discussed in Section 1.3, a consistent treatment of tangential friction between freely moving particles requires the inclusion of particle spins, which allows for energy transfer between random and rotational motions. Another way of inducing particle rotation, namely small scale surface irregularity is also examined.

With the addition of frictional dissipation the steady-state velocity dispersion is reduced, the importance of this reduction depending on both the value of  $\varepsilon_t$  and the model for  $\varepsilon_n$ . This is illustrated in Fig. 1.16, comparing different  $\varepsilon_t$  values for 'frosty' and 'smooth' ice elasticity models. A fixed  $\tau = 0.5$  is studied, but the relative effects is only weakly dependent on  $\tau$ . The influence of  $\varepsilon_t$  is much more pronounced for the dynamically hot 'smooth' ice model. This follows since the energy gain is determined by the local viscosity. Inclusion of friction adds a dissipation term proportional to  $\omega_c c^2(1 - \varepsilon_t^2)$  to Eq. (1.111), which means that the effective  $\varepsilon_n$  required for thermal balance can be closer to unity,

thus indicating smaller  $c$ . The extra dissipation is most pronounced when  $\varepsilon_t$  is close to zero, leading to minimum of  $c$  near this value. On the other hand, a much smaller adjustment in  $c$  is possible when the balance is dominated by nonlocal viscosity ('frosty' ice model in the figure).

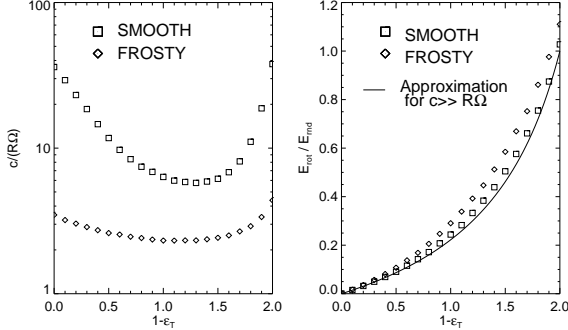


**Figure 1.16** Effect of tangential coefficient of restitution  $\varepsilon_t$  on a) the steady-state velocity dispersion, and b) the energy ratio between the rotation and random velocities. The 'frosty' and 'smooth' ice elasticity models are compared for  $\tau = 0.5$ . The solid line is the theoretical approximation (Eq. 1.115) for the energy ratio in the limit  $c \gg R\Omega$ .

Friction also induces spin motion of particles, which provides a feedback of energy from rotation to random motions (explains why the minimum of  $c$  is not exactly at  $\varepsilon_t = 0$ ). An equilibrium ratio between random and rotational energies is established when the net transfer equals zero. In practice the equilibrium implies that the dispersion of the surface velocities due to spins follows the dispersion of random velocities

$$\overline{(R\omega)^2} = k \overline{c^2}, \quad (1.113)$$

the proportionality factor  $k$  depending mainly on  $\varepsilon_t$ , and to lesser degree on  $\varepsilon_n$  and  $\tau$ . For a thick multilayer system the resulting equilibrium ratio of spin and random energies can be estimated by averaging the formula for the change of spin energy in individual impacts (Eq. 1.43), and by assuming an isotropic distribution of impact directions (should be valid in the case  $c \gg R\Omega$ ). For homogeneous spheres with

$$E_{rot} = \frac{1}{5}m(q_1^2 + q_2^2 + q_3^2) \quad (1.114)$$

$$E_{rnd} = \frac{1}{2}m(c_1^2 + c_2^2 + c_3^2)$$

this yields (Salo 1987a,b, Morishima and Salo (2006))

$$\frac{E_{rot}}{E_{rnd}} \approx \frac{2(1 - \varepsilon_t)}{14 - 5(1 - \varepsilon_t)}, \quad (1.115)$$

indicating that the energy ratio grows roughly proportional to  $1 - \varepsilon_t$  for  $\varepsilon_t$  close to unity. At the limit  $\varepsilon_t \rightarrow -1$  a total equipartition between rotation and random energies is predicted, in agreement with Shu and Stewart (1985). Based on Fig. 1.16 this approximation holds quite well for the 'smooth' ice model, especially in the limit  $|\varepsilon_t| \rightarrow 1$  where

the system has the largest velocity dispersion. For a more flattened system ('frosty') the simulated  $E_{rot}/E_{rnd}$  ratio is somewhat larger, reflecting the non-isotropic orientations of impact directions.

In addition to dispersion of spins, the particles also acquire a small residual mean vertical spin

$$\overline{\omega_z} \sim (0.2 - 0.3)\Omega \quad (1.116)$$

(Salo 1987a, 1987b, Morishima and Salo 2006). This mean value is only weakly dependent on  $\varepsilon_t$ ,  $\varepsilon_n$  or  $\tau$ . Since  $\sqrt{\omega_z^2}$  is proportional to  $c/R$  while  $\overline{\omega_z}$  is independent of  $c$ , the ratio  $\overline{\omega_z}/\sqrt{\omega_z^2}$  can be significantly non-zero only for very flattened systems with small  $c/(R\Omega)$ .

### 1.8.1.5 Surface irregularity/deviations from spherical shape

Almost all planetary ring simulations have assumed spherical particles. Mainly this is due to the technical simplifications it affords for detection and modeling of impacts. Also, the need for more complicated models is not obvious, since in many respects the effect of small deviations from spherical shape can be expected to average out, or to be accommodated by the uncertainties in the other model parameters like the elasticity of particles. However, irregular shape may have a significant contribution to particle spins, even if the tangential friction is small.

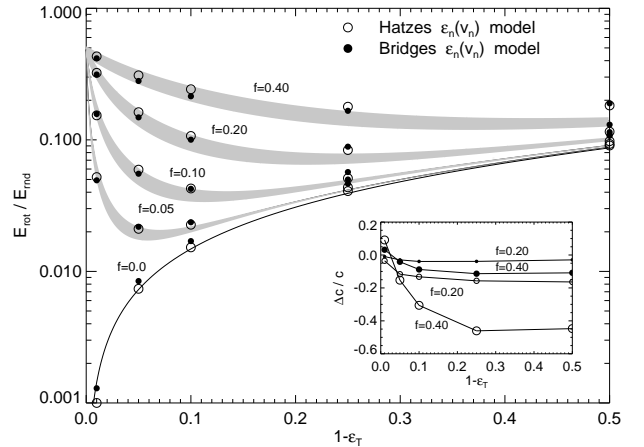


**Figure 1.17** The effect of small irregularities/deviation from spherical shape on the energy ratio between rotation and random motions. Simulations with different  $f$  (the maximum local tilt of the impact plane, see the text) are compared as a function of  $\varepsilon_t$  for two  $\varepsilon_n(v_n)$  models. The optical depth  $\tau = 0.5$ . The theoretical energy ratio for mass point systems, Eq (1.117) applies to a constant  $\varepsilon_n$ : the gray filled areas correspond to this approximation with  $\varepsilon_n = 0.5 - 0.8$ . The insert shows the relative change in velocity dispersion  $c$  compared to the case  $f = 0$ . Two values of  $f$  are compared (larger symbols  $f = 0.4$ , smaller symbols  $f = 0.2$ ).

The effect of slightly non-spherical shape in promoting spin dispersion is illustrated in Figure 1.17, in terms of the energy ratio between rotation and random motions. The

simulations use the irregularity model of Salo (1987a, b), where the normal vector of the local tangent plane of impact ( $\vec{k}^*$ ) deviates slightly from the direction vector joining the particle centers ( $\vec{k}$ ). In the figure the tilts  $\gamma_a$  and  $\gamma_b$  in Eq. 1.44 are assumed to get independent random values uniformly from the interval  $[-f, f]$ : the maximum studied value  $f = 0.4$  corresponds to rms tilt angle  $\sim 10^\circ$ . Such a model is very efficient in promoting spin dispersion even if the particles are almost frictionless: for example  $\varepsilon_t = 0.99, f = 0.05$  (corresponds to  $\sim 1^\circ$  rms tilt) induces about the same amount of spin rotation than  $\varepsilon_t = 0.5$  for spherical particles with  $f = 0$ . Curiously enough, the energy ratio at the limit  $\varepsilon_t \rightarrow 1$  is independent of  $f$ . The figure also shows an estimate of the equilibrium energy ratio (again setting the net transfer to zero; Salo 1987a), which is in good agreement with the simulation results,

$$\frac{E_{rot}}{E_{rnd}} = \frac{2}{7} \frac{\frac{2}{3}f^2(\varepsilon_t + \varepsilon_n)(1 + \varepsilon_n) + \frac{1}{2}(1 - \varepsilon_t)^2}{(1 - \varepsilon_t) + \frac{2}{3}f^2(\varepsilon_t + \varepsilon_n) - \frac{5}{14}(1 - \varepsilon_t)^2} \quad (1.117)$$

The theoretical estimate is for a constant  $\varepsilon_n$ , but the dependence on  $\varepsilon_n$  is weak (see Fig. 1.17) This agrees with the fact that the simulated  $E_{rot}/E_{rnd}$  are very similar for both studied  $\varepsilon_n(v_n)$  models. At the limit  $\varepsilon_t = 1$  this approximation predicts  $E_{rot}/E_{rnd} = \frac{2}{7}(1 + \varepsilon_n) \sim 0.5$ .

Irregularity also affects the equilibrium velocity dispersion, the effect depending on  $\varepsilon_t$  and  $\varepsilon_n$  (see the insert in Fig.1.17). In the case of hot system ('smooth' ice  $\varepsilon_n(v_n)$  model), the reduction for  $f = 0.4$  is close to 50% for  $\varepsilon_t < 0.8$ . However, for  $\varepsilon_t$  very close to unity, irregularity may also slightly increase the steady-state velocity dispersion: the reduced energy dissipation is then due to feedback of energy from rotation (Salo 1987b). For cool systems ('frosty' ice  $\varepsilon_n(v_n)$  model) the effect of irregularity, like that of friction, is much smaller.

### 1.8.1.6 Size distribution

So far all our simulation examples have assumed identical particles. In the more realistic case of size distribution, the energy balance is modified by the energy transfer in impacts (and via gravitational encounters) from larger to smaller particles (see Stewart et al. (1984), Hämeen-Anttila (1984)). However, in contrast to gas dynamical systems this tendency toward energy equipartitioning is opposed by the inelasticity of impacts: simulations indicate that near equipartition is possible only for particle mass ratios below about 10 (Ohtsuki 1991, Salo 1992a). In practice the ratio between velocity dispersion of smallest and largest is less than about 5, the maximum ratio depending on the functional form of the size distribution and the elasticity model.

Figure 1.18a shows how the vertical thickness  $H$  of different sized particles depends on the width  $W = R_{max}/R_{min}$  and index  $q$  of the power-law size distribution with  $dN/dR \propto R^{-q}$ . A constant  $\varepsilon_n = 0.5$  is used, in which case all simulation quantities scale with the assumed maximum particle size. Therefore, quantities normalized to  $R_{max}$  are shown. For  $q = 3$  the maximum ratio in the vertical thickness of the bin of smallest and largest particles ( $H_{small}/H_{large}$ ) depends

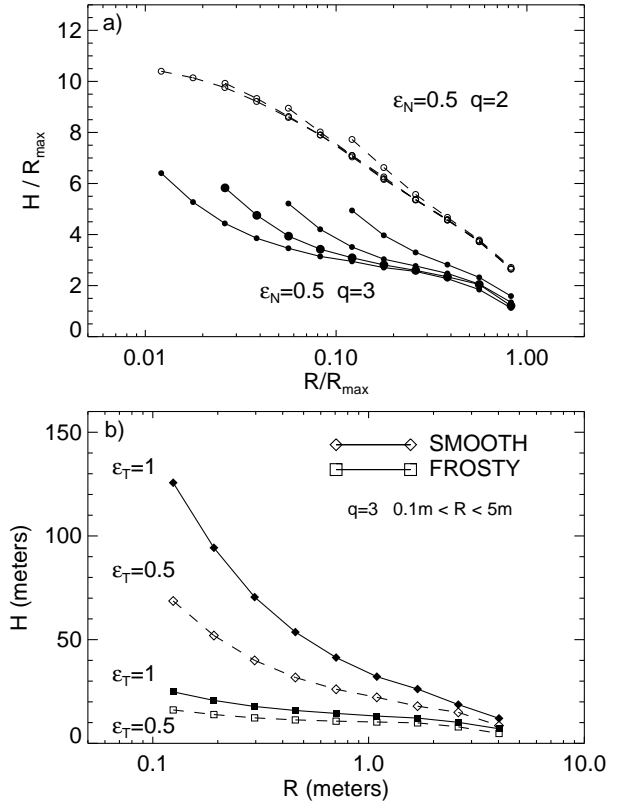


**Figure 1.18** In a) the geometric thickness as a function of particle size in simulations with a power law size distribution,  $dN/dr \propto r^{-q}$ , for  $R_{min} < R < R_{max}$ . Different widths of the distribution,  $W = R_{max}/R_{min}$ , in the range  $W = 4.64 - 100$  are compared, both for  $q = 2$  and  $q = 3$ . In each case  $\tau = 1.0$  and a constant  $\varepsilon_n = 0.5$  is used. In b) two different  $\varepsilon_n(v_n)$  models are compared for the same size distribution. Dashed lines show the effect of friction with  $\varepsilon_t = 0.5$ .

only weakly on  $W$ , while for  $q = 2$  it slightly increases with  $W$ . For  $q = 2$  most of the mass is on the largest particles: consequently the influence of small particles on the largest particles is small and  $H_{large}$  is independent of  $W$ . For  $q = 3$  each logarithmic size increment corresponds to same fraction of total mass, and increasing the width  $W$  pushes  $H_{large}$  down. The lower panel of Fig. 1.18 compares the two different  $\varepsilon_n(v_n)$  models for  $q = 3, W = 50, R_{max} = 5\text{m}$ , emphasizing how the separation between small and large particles becomes stronger for hot systems. In terms of steady-state velocity dispersion, the  $c_{small}/c_{large} \approx H_{small}/H_{large} \approx 10$  for the 'smooth' model, and about 3 for the 'frosty' ice. For comparison, for a constant  $\varepsilon_n \rightarrow 0$ , the  $c_{small}/c_{large} \approx 1.5$ . All simulations of Fig.1.18 have  $\tau = 1.0$ , but the results are only weakly dependent on  $\tau$  (Salo 1992a).

The effect of friction on  $c$  is roughly the same on all particle size bins (dashed lines in Fig. 1.18b). Also the equilibrium dispersion of surface spin velocities,  $(R\omega)^2$  scales with  $c^2$  of the size bin. The relatively weak dependence of  $c$  on  $R$  thus indicates that the spin dispersion  $\sqrt{\omega^2}$  is inversely proportional to particle radius, so that the small particles

spin much faster than the large ones. On the other hand, the residual mean spin is always a fraction of  $\Omega$  independent of particle size. Therefore, while the mean spin of the largest particles can be significant compared to its dispersion, the spin axis of the smallest ones are always practically randomly distributed. For an illustration of progradely rotating large particles embedded in a population of randomly oriented small particles, see Salo(1987b).

### 1.8.2 Self-Gravitating simulations

At low optical depth the main effect of self-gravity is through 2-body scattering in close binary encounters. Although they correspond to completely elastic impacts in the sense that they conserve the kinetic energy of the encountering pair, the deflection of the orbits during encounter leads to energy transfer from systematic to random motions. This extra heating increases  $c$  until it becomes roughly comparable to the escape velocity of the particles (Safranov, 1969; Hämeen-Anttila, 1978; Cuzzi et al., 1979). For larger surface densities, the collective effects become increasingly important. For example, it is easy to show that in Saturn's dense B the vertical self-gravity exceeds the vertical component of the central force by large factor (Wisdom and Tremaine, 1988). Nevertheless, then also the planar components of gravity need to be taken into account, leading to strongly non-uniform density distribution.

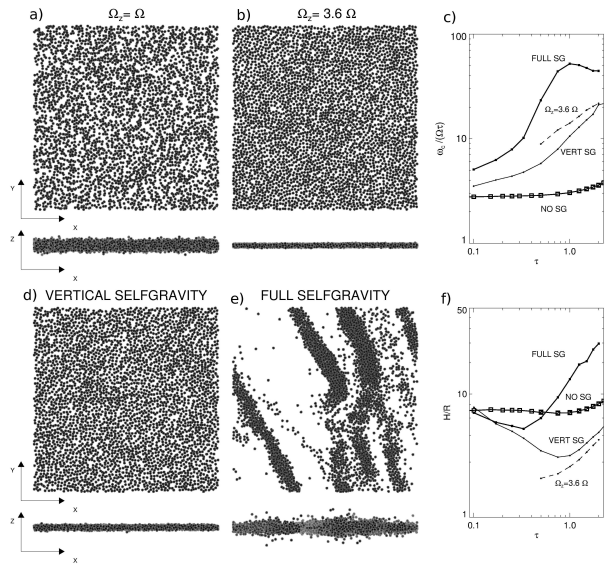
#### 1.8.2.1 Formation of self-gravity wakes

Figure 1.19 compares different ways to approximate ring self-gravity: using  $\Omega_z/\Omega > 1$  to mimic the increased vertical field and including the self-consistently calculated  $F_z$ . Clearly, a right choice of  $\Omega_z/\Omega > 1$  (depending on the surface density) would capture quite well the effects of vertical gravity: the flattening of the ring and the strongly enhanced impact frequency. However, with the inclusion of full self-gravity (Fig. 1.19d) the picture is completely different from that when only the vertical component of self-gravity is taken into account. The system now forms gravitational condensations which shear into elongated trailing density enhancements. Such structures, in the context of Saturn's rings, were first simulated in Salo (1992a). However, the phenomenon itself was envisioned already a few decades earlier, in the context of galaxy disks.

Toomre (1964) showed that a self-gravitating differentially rotating disk is locally unstable against the growth of axisymmetric disturbances if its radial velocity dispersion falls below a critical value. The closeness to the stability boundary is measured by the Toomre  $Q$  parameter

$$Q = \frac{c_x}{c_{cr}} = \frac{c_x \kappa}{3.36 C F \Sigma} \quad (1.118)$$

where  $c_x$  is the radial velocity dispersion. While  $Q \geq 1$  guarantees stability against the growth of *axisymmetric* perturbations, already for  $Q \lesssim 2 - 3$  the system is susceptible to the growth of local *non-axisymmetric* disturbances (Julian and Toomre, 1966; Goldreich and Lynden-Bell, 1965). Such a near-instability manifests as the emergence of trailing filamentary density enhancements just as those seen in



**Figure 1.19** Snapshots from  $2\lambda_{cr} \times 2\lambda_{cr}$  simulations with  $\tau = 0.75$ , using the 'frosty' ice elasticity model. In the upper row non-gravitating simulations with a)  $\Omega_z/\Omega = 1$  and b)  $\Omega_z/\Omega = 3.6$ . In the lower left, in d) the vertical component of self-gravity is self-consistently included, while e) the full self-gravity is taken into account. The internal density  $\rho = 900\text{kgm}^{-3}$  which corresponds to  $r_h = 0.82$  at the simulated Saturnocentric distance 100 000 km (see Eq. 1.122). Also shown in c) is the impact frequency (normalized by  $\tau\Omega$  and in f) the vertical thickness (averaged over the whole system) as a function of optical depth.

the self-gravitating simulations. As illustrated in Sect. 1.4, in Keplerian velocity field such wakes form  $\sim 15^\circ - 20^\circ$  angle with respect to the tangential direction, and their radial separation is of the order of Toomre's critical wavelength

$$\lambda_{cr} = 4\pi^2 G\Sigma/\kappa^2. \quad (1.119)$$

Individual filaments are continuously destroyed by shear, but new condensations are continuously regenerated. Due to enhanced densities and systematic motions associated with the wakes, the  $\omega_c$  is even more strongly enhanced than in the case of vertical gravity (Fig. 1.19c). Also, the vertical thickness increases as the scattering by wakes more than compensates the flattening by the vertical field (Fig. 1.19f).

Figure 1.20 illustrates the role of wakes/impacts in establishing a 'thermostat' which keeps the system near a constant  $Q$  regardless of the initial state of the system. In the case of stellar disks, originally studied by Toomre, the gravitational scattering accompanying the growing disturbances heats the system so that the wakes are eventually suppressed. In the case of particulate rings, the collisional dissipation provides a natural physical regulating mechanism which makes it possible to reach and maintain a statistical steady-state with sufficiently low  $Q$ , so that new structures continuously emerge and dissolve in a timescale comparable to the orbital period. As emphasized by Toomre and Kalnajs (1991), the gravity wakes do not represent an instability in the sense that there would be a strict threshold for the emergence of the wakes - rather they manifest

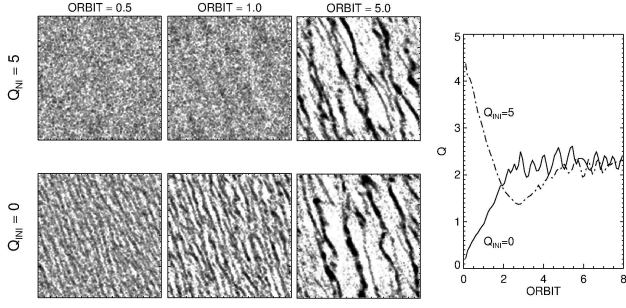


**Figure 1.20** Establishment of statistical steady-state in  $8\lambda_{cr} \times 8\lambda_{cr}$  simulations starting from a hot ( $Q = 5$ ) and cold ( $Q = 0$ ) uniform initial state. The parameters are  $\tau = 0.5$ ,  $r_h = 0.82$ ,  $\varepsilon_n = 0.5$ .

the enhanced reactivity of the selfgravitating disk whenever  $Q$  is sufficiently small. In particular, any small leading perturbation, while evolving into a trailing one due to shear, is significantly amplified by the interplay of gravity and differential rotation (the ‘swing amplification’ mechanism, see Toomre (1981); Goldreich and Lynden-Bell (1965).

The self-gravity structures seen in simulations can be interpreted as a superposition of numerous individual Julian and Toomre (1966) wakes, excited by each particle when other particles flow past it - this justifies the name (‘wake’) commonly adopted to the phenomenon. This identification is supported by the 2D auto-correlation analysis of the simulated self-gravity wakes (Toomre and Kalnajs, 1991; Salo, 1995; Salo et al., 2004; Michikoshi et al., 2015). To further strengthen the argument, Fig. 1.21 compares auto-correlation functions from ring simulations with the Julian and Toomre (1966) theoretical calculations of the density response around an orbiting mass enhancement, performed for different central shear rates. The trend in the pitch angle of the density crest as a function of  $s\Omega$  is strikingly similar. Also as expected, the scale of structures is in all cases proportional to  $\lambda_{cr}$ , which is different by a factor of 3 for the studied shear rates ( $\lambda_{cr} \propto \kappa/\Omega^{-2} = (2s/\Omega + 4)^{-1}$  according to Eq. (1.6)). More quantitative comparison is not attempted, as the Julian and Toomre (1966) response-calculations assumed a fixed  $Q$  for the disk and do not account for the finite particle size - in simulations of Fig. 1.21 the velocity dispersions adjusts self-consistently to balance the dissipation and viscous gain.

### 1.8.2.2 Survey of self-gravity wakes

In the non-gravitating case the optical depth  $\tau$  and the elasticity model determine the ring steady-state for a given particle size distribution (see Sect. 1.8). When self-gravity is included, just one additional parameter is required to characterize both the pairwise and collective gravitational effects. This is the  $r_h$  parameter, the ratio of the mutual Hill-radius for a pair of particles to the sum of their physical radii,

$$r_h(\mu) = \frac{R_{Hill}}{R_1 + R_2} = \left( \frac{\rho}{3\rho_{plan}} \right)^{\frac{1}{3}} \left( \frac{r}{r_{plan}} \right) \frac{(1 + \mu)^{\frac{1}{3}}}{1 + \mu^{\frac{1}{3}}} \quad (1.120)$$

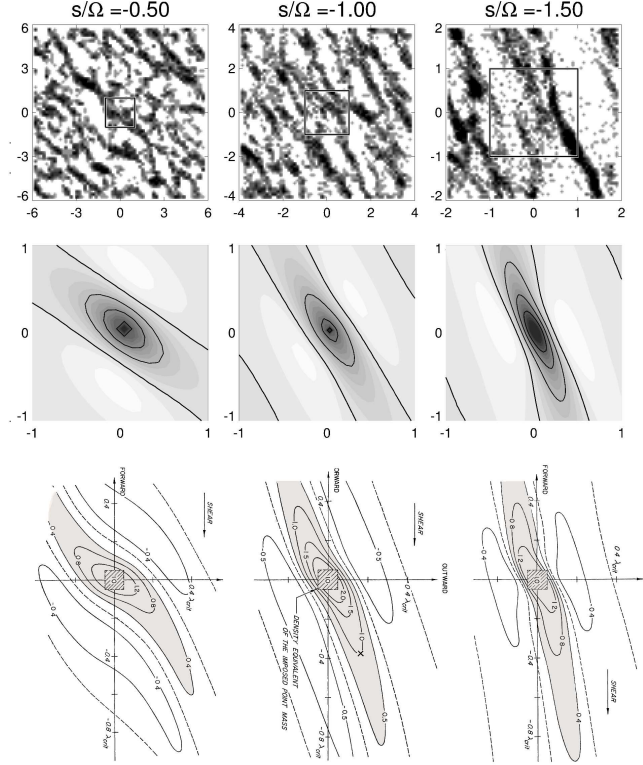


**Figure 1.21** The upper row shows snapshots from simulation with different shear  $s$ : the physical width of the calculation region is fixed ( $\sim 170$  particle radii) and corresponds to 12, 8, and  $4\lambda_{cr}$  for  $s/\Omega = -0.5, -1.0$  and  $-1.5$ . The middle row shows 2D auto-correlation plots from the same simulations, covering  $2\lambda_{cr} \times 2\lambda_{cr}$ . The lowermost row shows Julian-Toomre (1966) analytical calculations for the same shear rates of the wake response around an orbiting point mass-point: their graphs have been rotated to same orientation as our simulation plots. In the simulations  $\tau = 0.5$ , constant  $\varepsilon_n = 0.5$ ,  $r_h = 0.82$ .

where  $\rho$  is the internal density of the particles, and  $\mu = M_1/M_2 = (R_1/R_2)^3$  is their mass ratio. Here

$$R_{Hill} = ((M_1 + M_2)/3M_{plan})^{1/3} r \quad (1.121)$$

is the radius of the Hill-sphere, inside which the pair’s mutual gravity dominates over the tidal pull from the planet at the distance  $r$ . When  $r_h$  decreases, the particle pair extends more and more out from its Hill-sphere:  $r_h = 0$  corresponds to the non-gravitating case, while if  $r_h = 1$  the attraction between two synchronously rotating, radially aligned ring particles in contact equals the disruptive tidal force. For a pair of identical particles  $\mu = 1$ , and inserting the typical numerical values for Saturn’s rings gives

$$r_h(\mu = 1) = 0.82 \left( \frac{M_{plan}}{5.69 \cdot 10^{26} \text{ kg}} \right)^{-\frac{1}{3}} \left( \frac{\rho}{900 \text{ kgm}^{-3}} \right)^{\frac{1}{3}} \left( \frac{r}{100 \text{ 000 km}} \right). \quad (1.122)$$

We will denote  $r_h(\mu = 1)$  simply by  $r_h$ . For  $\mu = 0$  or  $\mu \rightarrow \infty$  (a test particle attached to surface of a large particle), the

$r_h$  would be a factor  $2^{2/3} \approx 1.59$  larger. With the formula 1.122, the simulation results for a given  $r_h$  can be scaled to any other  $\rho^{1/3}r$  combination.

To demonstrate that  $r_h$  is the only additional parameter needed to characterize self-gravity wakes, we may write the Toomre critical wavelength and velocity dispersion as

$$\frac{\lambda_{cr}}{R} = 48\pi \tau r_h^3, \quad (1.123)$$

$$\frac{c_{cr}}{R\Omega} = 12.8 \tau r_h^3. \quad (1.124)$$

Here we have assumed identical parameters; in case of size distribution the numerical prefactors would depend on  $dN/dR$ . Similarly, the minimum velocity dispersion maintained by gravitational encounters,  $c_{enc} \sim v_{esc}$ , where  $v_{esc} = \sqrt{2GM/R}$  is the 2-body escape speed. This can be expressed as

$$\frac{c_{enc}}{R\Omega} = 4.9 r_h^{3/2} \quad (1.125)$$

Figure 1.22a depicts a simulation surveys of wake structures for the 'frosty' ice elasticity model. The strength of wakes increases when the optical depth  $\tau$ , or the distance (measured with  $r_h$ ) increases: distinct wakes are seen with all the studied optical depths  $\tau \geq 0.25$ . The wakes get clumpier and eventually degrade into semi-permanent gravitational aggregates for  $r_h \gtrsim 1.2$ . Same takes place at low  $\tau$  via pairwise accumulation. The exact boundary for aggregate formation depends on the elasticity of particles and also the particle size distribution (Salo, 1995; Karjalainen and Salo, 2004). The fact that  $r_h > 1$  is required for stable aggregates to form is because not only shear, but also particle impacts and velocity dispersion act to destroy any forming condensations.

The insert in Fig. 1.22a sketches the parameter regimes where different factors (impacts, encounters, wakes) dominate the dynamics, based on the velocity dispersion this factor alone would be able to maintain (Salo, 1995; Ohtsuki and Emori, 2000). For the frosty ice model (or constant  $\varepsilon_n \lesssim 0.5$ ) the minimum velocity dispersion due to impacts is

$$\frac{c_{imp}}{R\Omega} \sim 2 - 3 \quad (1.126)$$

Comparing to Eq. (1.125), we may expect that velocity dispersion is governed by gravitational encounters rather than by physical impacts for  $r_h \gtrsim 0.7$ . A rough criterion for the emergence of collective wake-structure is obtained by assuming that wakes become apparent whenever the minimum velocity dispersion drops below  $c_{wake} = Q c_{cr}$  with  $Q \sim 2$ . According to Eqs. (1.124) and (1.126) this corresponds to  $\tau r_h^3 \gtrsim 0.1$ . In the insert figure the condition  $c_{wake} > c_{imp}$  (and  $c_{wake} > c_{enc}$ ) defines the sketched boundary between wakes and impacts (or wakes and encounters). The other dashed curves in the insert indicate where  $Q = 2$  corresponds to  $c/(R\Omega) = 5, 10, 20$ .

Figure 1.22b shows a similar survey, except with the 'smooth ice' elasticity model. No wake structures are visible for optical depths  $\tau = 0.25$  or  $\tau = 0.50$  for any  $r_h$ , but for higher  $\tau$  the picture is very similar to that in a). The reason for the suppression of wakes at low  $\tau$  is the high velocity dispersion maintained by impacts alone: according to

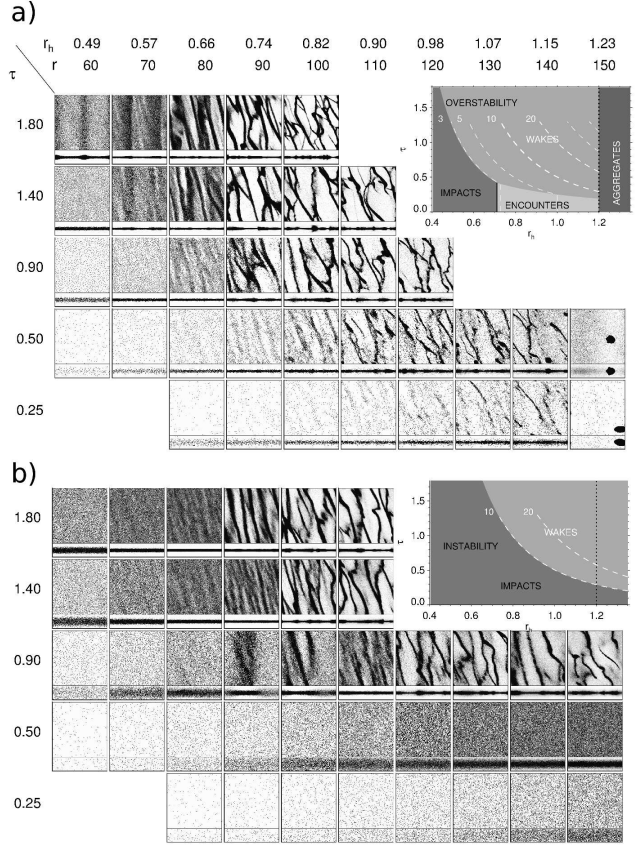


**Figure 1.22** Survey of self-gravity wakes as a function of  $r_h$  and  $\tau$ . The labels  $r$  indicate the Saturnocentric distance (in units of 1000 km) for particles with solid ice internal density: for other densities the distances scale  $\propto (\rho/900\text{kgm}^{-3})^{-1/3}$ . The size of the simulation system is  $4\lambda_{cr} \times 4\lambda_{cr}$ , with  $\lambda_{cr}/R \approx 150\tau r_h^3$ , the side view covers  $4\lambda_{cr} \times 1\lambda_{cr}$ . The number of simulation particles  $N \approx 116 \cdot 10^3 \tau^3 r_h^6$ . In a) the 'frosty' ice and in b) the 'smooth' ice elasticity model is used. Note that a constant  $\varepsilon_n \lesssim 0.5$  yields rather similar results (compare with similar  $\varepsilon_n = 0.5$  survey in Salo (2012)). The inserts sketch the regimes where various physical factors dominate, based on the estimates given in the text. The dashed curves indicate what is the radial velocity dispersion which corresponds to  $Q = 2$ : in a) the boundary between wakes and impacts is drawn at  $c_r/(R\Omega) = 3$ , while in b)  $c_r/(R\Omega) = 10$  is assumed. Note the region  $\tau \gtrsim 1$  and  $r_h \lesssim 0.6$  in a) leading to viscous overstability (see Sect. 1.9.1). Similarly in b) simulations with  $\tau = 0.9$ ,  $r_h \sim 0.8$  show viscous instability (see Sect. 1.9.2).

Fig. 1.14, we have  $c/(R\Omega) > 10$  for  $\tau \lesssim 1$ . In the inset figure this value is used to delineate the boundary between impacts and wakes. Now the velocity dispersion of the system is too high to allow for bound aggregates to form at any of the studied  $r_h$ 's.

The wake structure is also affected by the particle size distribution (Fig. 1.23). Although the large particles still form distinct wakes, the overall contrast is reduced due to the more uniform distribution of small particles. This implies that a system can exhibit dynamically significant wake structure, though it might be more hidden in photometric observations (Salo et al., 2004).

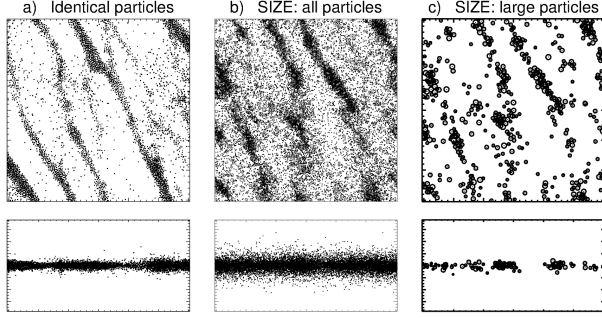


**Figure 1.23** a) Identical particle simulation with  $\tau = 0.5$ ,  $r_h = 0.85$ , using ‘frosty’ particle elasticity model. b) Simulation with same parameters, except having a  $q = -3$  power-law size distribution with  $R_{max}/R_{min} = 10$ . c) Particles with  $R > R_{max}/2 = 2.1$  meters are shown separately: they comprise 30% of the optical depth and 55% of surface mass density.

### 1.8.2.3 Gravitational viscosity

The effect of gravity wakes on viscosity is depicted in Fig. 1.24. The upper row compares self-gravitating simulations with constant  $\varepsilon_n = 0.5$  as a function of both  $r_h$  and  $\tau$ . For  $\tau \gtrsim 0.5$  and  $r_h \gtrsim 0.75$ , the  $\nu_{grav}$  contribution associated with the gravitational torques from inclined wakes become dominant (Daisaka et al., 2001; Tanaka et al., 2003). Also  $\nu_{local}$  is strongly enhanced due to systematic motions associated with the wakes, whereas the  $\nu_{nl}$  has less significance. The results of Fig. 1.24 agree with the trend originally found in Daisaka et al. (2001),

$$\nu_{tot} \approx (\nu_{grav} + \nu_{local}) \approx 2\nu_{grav} \propto \frac{r_h^5 G^2 \Sigma^2}{\Omega^3}. \quad (1.127)$$

The  $\Sigma^2$  ( $\propto \tau^2$  in the figure) dependence is similar to the standard continuum fluid formula for spiral torques in galaxy disks (Lynden-Bell and Kalnajs, 1972), while the  $r_h$  dependence can be interpreted as an extra effect related to the finite size of particles: the smaller the  $r_h$ , the closer is the scale of wakes compared to physical size of particles (see Eq. 1.123). This limits the maximum contrast the wakes can attain as the density of wakes is limited by the internal density of particles. The slope of  $\nu(\tau)$  relation is shown in more detail in Fig. 1.24d and also compared with non-gravitating simulations and to simulations including only the vertical component of self-gravity (compare to Fig. 1.19). With the inclusion of only vertical gravity the slope  $\beta \gtrsim 1$  for  $\tau \gtrsim 1$  is clearly smaller than with full-self-gravity, but still higher than in the non-gravitating case ( $\beta \approx 0.5$ ). Note that when using  $\Omega_z/\Omega$  to mimic vertical gravity,  $\beta$  can be increased by choosing a larger enhancement factor.

Based on Figure 1.22 it is clear that the gravitational viscosity depends strongly on the used elasticity model. In Fig. 1.24c this is illustrated by comparing simulations with different  $\varepsilon_n(v_n)$  models, parameterized by the velocity scale factor in the Bridges et al (1984) type elasticity law (‘frosty ice’ model has  $v_c/v_B = 1$ , while the smooth ice model would correspond to  $v_c/v_B \sim 30$ ). The more inelastic the impacts are, the larger is the contribution from gravitational viscos-

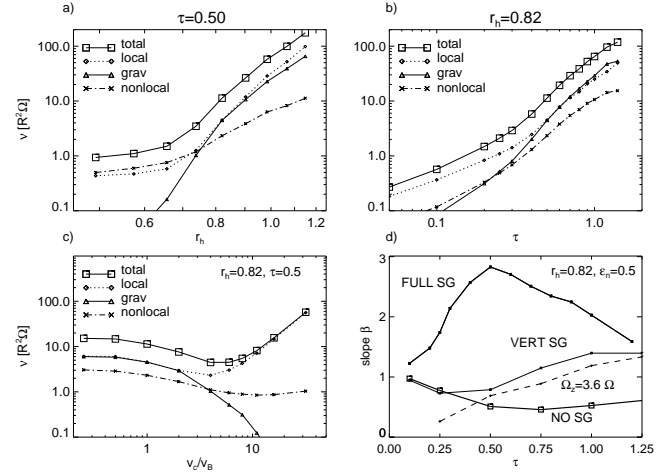


**Figure 1.24** Comparison of various contributions to total viscosity, in a) as a function of  $r_h$  and b) as a function of  $\tau$ . They are from a constant  $\varepsilon_n = 0.5$  simulations similar to Fig. 1.22. In c) the viscosity as a function of scale parameter  $v_c$  in velocity-dependent elasticity model  $\varepsilon_n(v_n) = (v_n/v_c)^{-0.234}$ ; with  $v_c = v_B = 0.000077m/s$  this corresponds to the Bridges et al. (1984) ‘frosty’ ice model. Frame d) displays the slope of  $\nu \propto \tau^\beta$  in simulations of frame b), reaching values  $\beta \approx 2 - 3$  in self-gravitating simulations; also non-gravitating simulations and simulations including only the vertical self-gravity are shown.

ity. For the simulated  $\tau = 0.5$ , the gravitational viscosity is completely negligible for  $v_c/v_B = 30$ , in agreement with the total absence of wake structure in the simulations depicted in 1.22b. At the same time for very elastic impacts the local viscosity increases proportional to  $(v_c/v_B)^2$ . This follows as the system tries to establish a thermal balance with a mean elasticity whose value depends on the optical depth via the Goldreich-Tremaine formula. The resulting steady-state  $c$  is proportional to  $v_c$  and thus  $\nu_{tot} \approx \nu_{local} \propto v_c^2$ . Because of the opposite trends of  $\nu_{local}$  and  $\nu_{grav}$ , and the relatively insignificant role of  $\nu_{nl}$ , the total viscosity has a minimum around  $v_c/v_B \approx 3$ .

## 1.9 Viscous instability and overstability

The Voyager and Cassini data have revealed overwhelming amount of structure in Saturn’s rings. Some of the structure is unambiguously connected to resonance perturbations by external satellites (in particular in the outer A ring), but the majority of the finest optical depth variations, extending down to shortest resolved length scales, are likely to have some internal origin.

Right after Voyager discoveries *viscous instability* was evoked to explain the intrinsic variations (Lukkari, 1981; Lin and Bodenheimer, 1981; Ward, 1981). In this type of instability (see Fig. 1.25), the collisional flux of particles, proportional to dynamic viscosity  $\eta = \nu\tau \propto \tau^{\beta+1}$ , is directed toward density maxima (equivalent to  $\beta < -1$ ). Thus any small density fluctuation is amplified by colli-

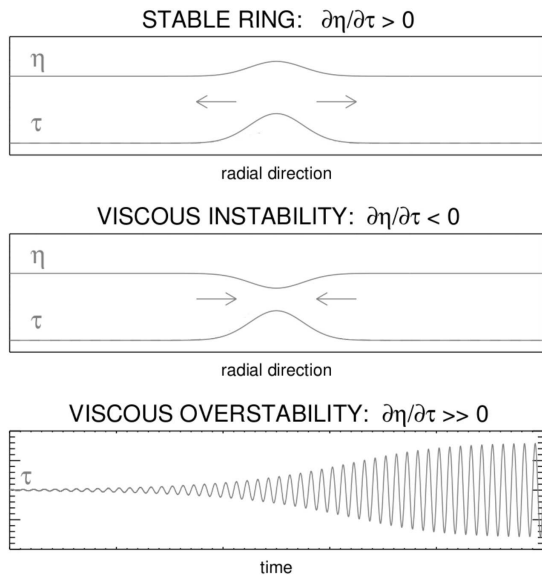


**Figure 1.25** Schematic illustration of viscous stability properties. The radial mass flux is proportional to  $-\partial\eta/\partial\Sigma$ , where  $\eta$  is the dynamic viscosity and  $\Sigma$  is the surface mass density. This indicates that the ring tries to establish a locally constant  $\eta$  profile. In stable ring  $d\eta/d\Sigma > 0$  so that local density fluctuation are smoothed, in contrast to  $d\eta/d\Sigma < 0$  which leads to *viscous instability*. However, if  $d\eta/d\Sigma \gg 0$  the suppression overshoots leading to periodic oscillations with amplitude growing with time until saturated at some finite value (*viscous overstability*). In case of non-selfgravitating system optical depth  $\tau$  replaces  $\Sigma$  and  $\eta$  is obtained from kinematic viscosity as  $\eta = \tau\nu$ .

sional diffususion, in contrast to a stable ring where diffusion smooths density variations. In the nonlinear limit the growth of fluctuations is saturated to a state where the flux from dense but dynamically cool ringlets is balanced by the flux from rarefied, dynamically hot regions. This model was soon discarded, mainly as the first laboratory measurements (Bridges et al., 1984) indicated too dissipative particles for the instability mechanism to work (Wisdom and Tremaine, 1988; Araki and Tremaine, 1986). Also, the observed structures do not quite agree with the predictions of simple instability models, according to which the ring should separate into high  $\tau$  ringlets surrounded by almost empty gaps (Hämeen-Anttila, 1978).

Other alternatives for explaining the ring fine structure gained more attention, among them the possibility that dense rings might be viscously overstable (Borderies et al., 1985). In the axisymmetric *overstability* the radial particle flux is directed away from density maxima, like in a stable ring (see Fig. 1.25). However, the flux now increases so strongly with density (large  $\beta$ ), that the system overshoots in trying to smooth the density variations: this leads to density oscillating with time. Although it appears unlikely that overstability could account for large scale structures in the densest rings (Latter and Ogilvie, 2010), there are clear indications of small-scale  $\sim 100$  meter axisymmetric oscillations in moderate  $\tau$  locations in the rings (Colwell et al., 2007;

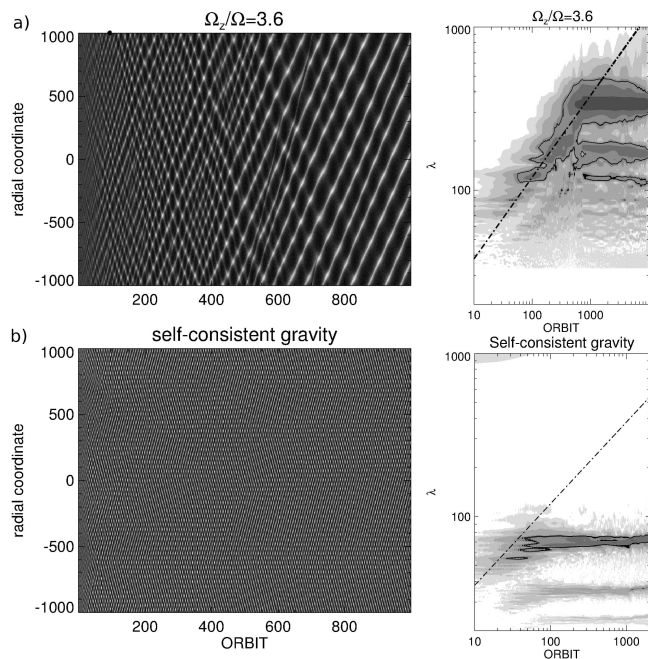


**Figure 1.26** Comparison of overstable oscillations in large-scale (2 km radial extent) non-gravitating and self-gravitating simulations ( $\tau = 1.2$ ,  $r_h = 0.7$ , 'frosty' ice). The frames in left show the evolution of the density profile with time, while in the right the amplitude spectrum ( $A_m(\lambda)$  in Eq. (1.72) is shown. In a) vertical self-gravity is mimicked with an enhanced  $\Omega_z/\Omega = 3.6$ . This leads to overstable oscillations whose radial wavelength grows until nonlinearly saturated  $\sim 500$  meter level. In b) gravity is treated self-consistently ( $\rho = 300\text{kg/m}^3$ ) and growth of overstable oscillations is limited to less than 100 meters. In the amplitude spectra the 10% contour is indicated with thick line. The dashed line in a) indicates the radial wavelength with the largest amplitude during the initial growth period. For comparison, the same line is also shown in b).

Thomson et al., 2007; Hedman et al., 2014) more likely to be related to such overstable oscillations.

### 1.9.1 Viscous overstability (Oscillatory instability)

Early hydrodynamical models for Saturn's rings predicted that practically any flattened ring system with  $\beta \gtrsim 0$  should be overstable (Schmit and Tscharnuter, 1995), leading to growing axisymmetric oscillations in density and velocity components. The mechanism itself can be confirmed in direct N-body simulations (Salo et al., 2001; Daisaka et al., 2001), which however indicate considerably more stringent conditions for the onset of overstability.

In non-gravitating simulations, and in simulations including vertical self-gravity, the condition (Salo et al., 2001; Schmidt et al., 2001)

$$\beta \gtrsim 1 \quad \text{overstability condition (non - gravitating)}$$

seems to provide a sufficient condition for overstability, provided that the size of the system exceeds the shortest scale of overstable oscillations, about 100 particle radii. For example,  $\beta > 1$  in the non-gravitating simulations with the 'frosty ice' elasticity model if  $\tau \gtrsim 4$  (Fig. 1.14d). Similarly,

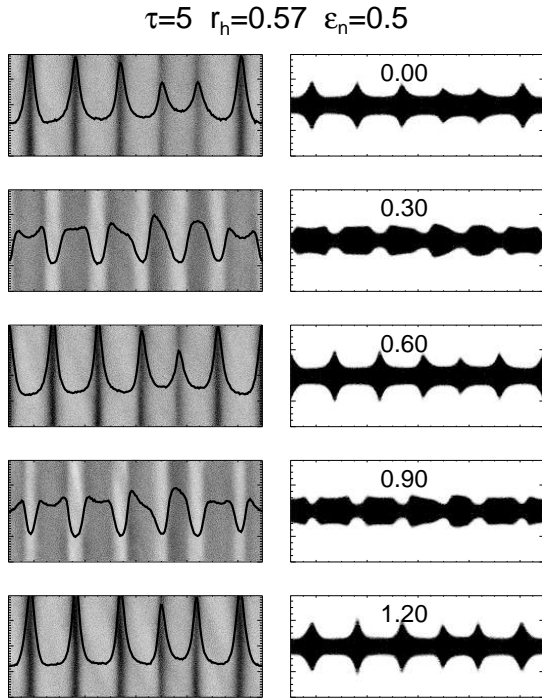


**Figure 1.27** Overstable oscillations followed over one full oscillation cycle ( $\sim 1.2$  orbital periods; the prolongation is due to self-gravity). The calculation region  $10\lambda_{cr} \times 2\lambda_{cr}$ . Note the vertical ‘splashing’ Borderies et al. (1985) associated with the density crests: the ring behaves in a nearly incompressible manner. The vertical scale in the plot is exaggerated by factor 5. Constant  $\varepsilon_n = 0.5$  with  $\tau = 5$ ,  $r_h = 0.57$

simulations where the vertical self-gravity is approximated with an enhanced vertical field  $\Omega_z/\Omega = 3.6$ , fulfil this condition for  $\tau \gtrsim 1$  (Fig. 1.24d). Indeed, in both cases simulations with sufficiently large calculation regions lead to spontaneous growth of overstable oscillations (Salo et al., 2001).<sup>6</sup>

Transport coefficients derived from simulations with different values of  $\Omega_z/\Omega$ , in combination with improved hydrodynamical models (Salo et al., 2001; Schmidt et al., 2001), have been useful in analyzing the linear growth rates of oscillations, and also in allowing analytical treatment of saturation in weakly nonlinear case (Schmidt and Salo, 2003). Significant progress has also been made using the kinetic theory approach (Latter and Ogilvie, 2008). recently, non-linear hydrodynamical analysis (Latter and Ogilvie, 2009, 2010) has shown that the wavelength growth of overstable oscillations is limited via interactions of traveling wavetrains at a few hundred meter to kilometer range, the maximum increasing with  $\beta$ . The non-gravitating, very large-scale simulations in Rein and Latter (2013) confirm this, and also demonstrate

<sup>6</sup> The same condition,  $\beta \gtrsim 1$  holds also in non-gravitating 2D simulations, where the steep rise of  $\nu_{nl}$  when the close-packing limit is approached, makes the system strongly overstable already for  $\tau \gtrsim 0.4$ . This fact was utilized in Salo (2001) to directly demonstrate overstability mechanism, before it was technically feasible in 3D simulations.

the richness of structure arising from the non-linear interaction of such wavetrains (ADD FIGURE).

However, it is still unclear what is the overstability condition for a fully self-gravitating rings. The simulations Salo et al. (2001) indicate that self-gravitating systems may exhibit overstability for  $\tau \gtrsim 1$ , but *only if the wake-structure is not too strong*. For example, in the survey of Fig. 1.22a, overstability is seen only in the upper left corner with  $r_h \lesssim 0.6$ . For stronger wakes the overstability is clearly suppressed, although the overstability condition for non-gravitating rings,  $\beta \gtrsim 1$ , should be satisfied with ample margin (see Fig. 1.24d). This suppression might be related to different phase and pitch angle of the velocity and density oscillations for overstability and wakes, combined with the fact that they occur at practically similar wavelength range. In any case, even an approximate analytical theory is missing, making fully self-gravitating numerical simulations indispensable in looking the interplay of wakes/overstability.

As mentioned above Rein and Latter (2013) have recently carried out simulations with radially very extended calculations regions (radial width even 50 km), facilitating the detailed study of interactions between non-linear wavetrains. However, these simulations use the  $\Omega_z/\Omega > 1$  approximation (Wisdom and Tremaine, 1988) to mimic self-gravity and it is therefore not clear how realistically they describe self-gravitating rings. Fig. 1.26 compares (a) this approximation with the (b) fully self-consistent gravity, in moderately large-scale simulations (radial width 2 km). In the former case the evolution is similar to Rein and Latter (2013) simulations, leading to formation of traveling wavetrains with increasing wavelengths, until a maximum scale of  $\sim 400$  meters is reached after about 1000 orbital periods. In the beginning several left and right traveling waves compete, but after about 500 orbits a single traveling wave dominates. The amplitude spectrum in the right indicates that no further wavelength evolution takes place during the span of the simulation (10000 orbits): the shorter modes represent the harmonics of the prevailing mode, related to its non-sinusoidal waveform.

In the self-gravitating simulation with same parameter values (Fig. 1.26b), the initial evolution is quite similar, in addition to weak wakes being superposed with the rapidly evolving axisymmetric overstable oscillations. However, the wavelengths of oscillations do not grow beyond about 100 meter level, although they should be ample time and spatial room for growth (see the amplitude spectrum). Unfortunately, such large-scale self-gravitating simulations are much more time-consuming than non-gravitating runs, since they must have also a tangential width sufficiently large to allow the gravity wakes properly evolve (the simulations with  $\Omega_z/\Omega > 1$  stay axisymmetric so their tangential width can be very narrow, see Rein and Latter (2013)).

Figure 1.27 illustrates overstable oscillations over one oscillation period in a dense system ( $\tau = 5$ ) with moderate strength of self-gravity ( $r_h = 0.57$ ). Unlike strong self-gravity wakes at larger  $r_h$ , both the maximum and minimum optical depths stay very high ( $\tau_{min} \gtrsim 2 - 3$ ). If this type of behavior is typical to the densest part of the B ring ( $r \sim 110\,000$  km), then according to the survey of Fig. 1.22

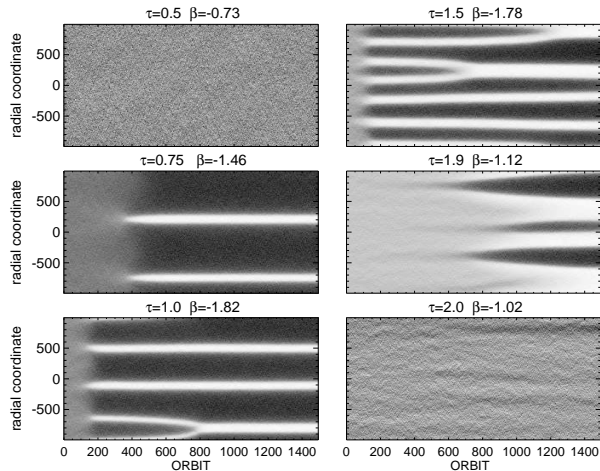


**Figure 1.28** Emergence of viscous instability in large-scale simulations (2km radial extent) using the ‘smooth’ ice elasticity model. The value of  $\beta$  is for the uniform initial state,  $\beta \leq -1$  indicates linear instability. Figure from Salo and Schmidt (2010)

the internal density should be order of  $\rho \sim 450\text{kgm}^{-3}$ , to yield  $r_h \approx 0.6$ . This would indicate the ring particles to be quite porous porous. Also, it would seem to rule out very elastic particles.

### 1.9.2 Viscous instability

In the case of viscous instability, the hydrodynamic stability criterion

$$\beta < -1 \quad \text{instability condition}$$

is fully consistent with direct N-body simulations (Salo and Schmidt, 2010), although the shortest unstable wavelengths ( $\sim 200$  particle radii) are about a factor of ten larger than what a simple hydrodynamical linear stability analysis predicts. Figure 1.28 displays large scale simulations which illustrate how the non-gravitating ‘smooth’ ice elasticity model leads to spontaneous amplification of density fluctuations for  $0.75 \lesssim \tau \lesssim 2$ , in very good agreement with the range of  $\tau$ ’s where the steady-state  $\beta < -1$  in small scale simulations of Fig. 1.14. The system is initially uniform and it takes about 100-500 orbital periods for random fluctuations to amplify to a nonlinear regime. Fig. 1.22b illustrates that viscous instability may arise also when self-gravity is included provided that  $\beta < -1$  (see the snapshots with  $\tau = 0.9, r_h \sim 0.7$ ).<sup>7</sup>

Figure 1.29 depicts in more detail the nonlinear steady-state after the saturation of the viscous instability. The state is characterized by a balance of radial particle flux between flattened dense ringlets surrounded by rarefied, large velocity dispersion regions, exactly as envisioned in Hämeen-Anttila (1978). The dynamic viscosity (obtained by tabulating pressure tensor separately at different radial zones)

<sup>7</sup> The same condition applies to 2D systems. Due to different functional form of impact frequency (see Sect. 1.8.1.1) hot 2D systems have  $\beta < -1$  at the limit  $\tau \rightarrow 0$ , which makes direct demonstrations of viscous instability numerically much easier than in 3d systems where  $\tau \sim 1$  is required (Salo, 2001; Salo and Schmidt, 2010).

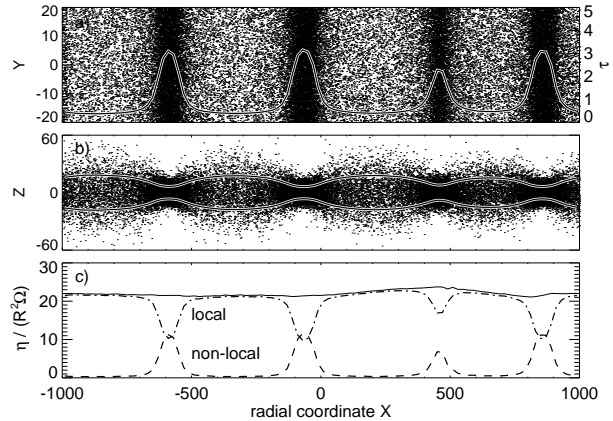


**Figure 1.29** Nonlinear radial balance between dense and rarefied regions resulting from viscous instability. The upper two frames show the top (a) and side views (b) of a simulation with  $\tau = 0.92$ , using the ‘smooth ice’ elasticity model. The frame c) depicts the dynamic viscosity profile (solid curve), showing separately the local and nonlocal contributions. Figure from Salo 2011.

has a nearly constant value through the simulation system. Note that one of the ringlets has a slightly lower  $\tau$  than the other three. This ringlet corresponds to a small bump in  $\eta$  and is accordingly slowly dissolving. With time, the ringlets slowly merge (see Fig 1.28), their typical separation growing  $\propto \sqrt{t}$ . In contrast to overstability, there is no mechanism known which would stop this growth. Thus at least in principle, large scale structure may emerge as a result of viscous instability.

Nevertheless, viscous instability is typically not regarded as a candidate for the ring fine-structure, basically since it requires fairly elastic particles in order to operate. In such a case the self-gravity wakes are harder to form. Also, the basic instability model in its simplest forms always requires a balance between a rarefied and a dense region, and thus, does clearly not apply, say, to the structure of the dense B ring.

#### 1.9.2.1 Selective viscous instability

There is a variant of the standard instability model that would allow both the minimum and maximum optical depths to be high, namely the possibility of a selective instability of small particles against the more uniform background of larger ones, first suggested in (Stewart et al., 1984). Direct simulations (Salo and Schmidt, 2010) indicate that such a situation is possible if the coefficient of restitution is smaller in impacts between small particles, than in impacts involving large particles. Such size-dependence of  $\varepsilon_n$  adds a new degree of freedom to the system, and in principle allows a balance of radial flux also between two dense regions. Importantly, the contrast can also have very different values depending on the details of the elasticity model assumed (Fig. 1.30). Nevertheless, this mechanism has yet been very little studied, and due to lack of relevant labora-

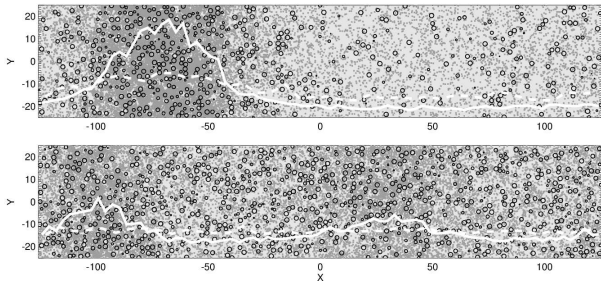


**Figure 1.30** Two examples of *selective viscous instability* in simulations (after 700 orbital periods). The systems consist of two particle sizes with  $R_2/R_1=3$ , and  $\tau_1 = \tau_2 = 0.5$ . Small (large) particles are indicated by gray (black) color, and the solid (dashed) white curve indicates their radial density profile. In the upper frame the impacts between small particles are much more inelastic than those between large particles, leading to strong density contrast among the small particles. In the lower frame the size-dependence of elasticity is smaller, leading to less pronounced variations. For exact parameter values, see Figs. 21 and 22 in Salo and Schmidt (2010).

tory measurements it remains unclear whether real particles possess suitable size dependence of  $\varepsilon_n$  leading to this type of instability.

## 1.10 Summary

## REFERENCES

- Araki, S. 1991. The dynamics of particle disks III. Dense and spinning particle disks. *Icarus*, **90**, 139–171.
- Araki, S., and Tremaine, S. 1986. The dynamics of dense particle disks. *Icarus*, **65**, 83–109.
- Borderies, N., Goldreich, P., and Tremaine, S. 1985. A granular flow model for dense planetary rings. *Icarus*.
- Brahic, A. 1977. Systems of colliding bodies in a gravitational field. I - Numerical simulation of the standard model. *Astron. & Astrophys.*
- Bridges, F.G., Hatzes, A.P., and Lin, D.N.C. 1984. Structure, stability and evolution of Saturn’s rings. *Nature*, **309**, 333–338.
- Burns, J.A., and Cuzzi, J. N. 2006. Our local astrophysical laboratory. *Science*, **312**, 1753–1755.
- Colwell, J. E., Esposito, L. W., and Sremčević, M. 2006. Self-gravity wakes in Saturn’s A ring measured by stellar occultations from Cassini. *Geophys. Res. Lett.*
- Colwell, J. E., Esposito, L. W., Sremčević, M., Stewart, G. R., and McClintock, W. E. 2007. Self-gravity wakes and radial structure of Saturn’s B ring. *Icarus*.
- Cundall, P. A., and Strack, O. D. L. 1979. A discrete numerical model for granular assemblies. *Geotechnique*, **29**, 47–65.
- Cuzzi, J. N., Durisen, R. H., Burns, J. A., and Hamill, P. 1979. The vertical structure and thickness of Saturn’s rings. *Icarus*, **38**, 54–68.
- Cuzzi, J. N., Burns, J. A., Charnoz, S., Clark, R. N., Colwell, J. E., Dones, L., Esposito, L. W., Filacchione, G., French, R. G., Hedman, M. M., Kempf, S., Marouf, E. A., Murray, C. D., Nicholson, P. D., Porco, C. C., Schmidt, J., Showalter, M. R., Spilker, L. J., Spitale, J. N., Srama, R., Sremčević, M., Tiscareno, M. S., and Weiss, J. 2010. An Evolving View of Saturn’s Dynamic Rings. *Science*, **327**, 1470–1475.
- Daisaka, H., and Ida, S. 1999. Spatial structure and coherent motion in dense planetary rings induced by self-gravitational instability. *Earth, Planets, and Space*.
- Daisaka, H., Tanaka, H., and Ida, S. 2001. Viscosity in a dense planetary ring with self-gravitating particles. *Icarus*.
- Dilley, J.P. 1993. Energy loss in collisions of icy spheres: Loss mechanism and size-mass dependence. *Icarus*, **105**, 225–234.
- Goldreich, P., and Lynden-Bell, D. 1965. II. Spiral arms as sheared gravitational instabilities. *Mon. Not. R. Astron. Soc.*, **130**, 125–+.
- Goldreich, P., and Tremaine, S. 1978. The velocity dispersion in Saturn’s rings. *Icarus*.
- Hämeen-Anttila, K. A. 1978. An improved and generalized theory for the collisional evolution of Keplerian systems. *Astrophys. Space Sci.*
- Hämeen-Anttila, K. A., and Lukkari, J. 1980. Numerical simulations of collisions in Keplerian systems. *Astrophys. Space Sci.*
- Hämeen-Anttila, K. A., and Salo, H. 1993. Generalized Theory of Impacts in Particulate Systems. *Earth, Moon & Planets*.
- Hatzes, A., Bridges, F. G., and Lin, D. N. C. 1988. Collisional properties of ice spheres at low impact velocities. *Mon. Not. R. Astron. Soc.*, **231**, 1091–1115.
- Hedman, M. M., Nicholson, P. D., Salo, H., Wallis, B. D., Buratti, B. J., Baines, K. H., Brown, R. H., and Clark, R. N. 2007. Self-gravity wake structures in Saturn’s A ring revealed by Cassini VIMS. *Astron. J.*
- Hedman, M. M., Burns, J. A., Evans, M. W., Tiscareno, M. S., and Porco, C. C. 2011. Saturn’s Curiously Corrugated C Ring. *Science*, **332**, 708–711.
- Hedman, M. M., Nicholson, P. D., and Salo, H. 2014. Exploring Overstabilities in Saturn’s A Ring Using Two Stellar Occultations. *Astron. J.*, **148**, 15.
- Julian, W. H., and Toomre, A. 1966. Non-axisymmetric responses of differentially rotating disks of stars. *Astrophys. J.*
- Karjalainen, R., and Salo, H. 2004. Gravitational accretion of particles in Saturn’s rings. *Icarus*.
- Latter, H. N., and Ogilvie, G. I. 2008. Dense planetary rings and the viscous overstability. *Icarus*.
- Latter, H. N., and Ogilvie, G. I. 2009. The viscous overstability, nonlinear wavetrains, and finescale structure in dense planetary rings. *Icarus*, **202**, 565–583.
- Latter, H. N., and Ogilvie, G. I. 2010. Hydrodynamical simulations of viscous overstability in Saturn’s rings. *Icarus*, **210**, 318–329.
- Lin, D. N. C., and Bodenheimer, P. 1981. On the stability of Saturn’s rings. *Astrophys. J. Lett.*, **248**, L83–L86.
- Lukkari, J. 1981. Collisional amplification of density fluctuations in Saturn’s rings. *Nature*, **292**, 433–435.
- Lynden-Bell, D., and Kalnajs, A.J. 1972. On the Generating Mechanism of Spiral Structure. *Mon. Not. R. Astron. Soc.*, **157**, 1–30.
- Makino, J., and Funato, Y. 1993. The GRAPE Software System. *Publications of the Astronomical Society of Japan*.
- Michikoshi, S., Fujii, A., Kokubo, E., and Salo, H. 2015. Dynamics of Self-gravity Wakes in Dense Planetary Rings. I. Pitch Angle. *Astrophys. J.*, **812**, 151.
- Morishima, R., and Salo, H. 2006. Simulations of dense planetary rings IV. Spinning self-gravitating particles with size distributions. *Icarus*.
- Ohtsuki, K. 1999. Evolution of particle velocity dispersion in a circumplanetary disk due to inelastic collisions and gravitational interactions. *Icarus*, **137**, 152–177.
- Ohtsuki, K., and Emori, H. 2000. Local N-Body Simulations for the Distribution and Evolution of Particle Velocities in Planetary Rings. *Astron. J.*
- Porco, C. C., Weiss, J. W., Richardson, D. C., Dones, L., Quinn, T., and Throop, H. 2008. Simulations of the dynamical and

- light-scattering behavior of Saturn's rings and the derivation of ring particle and disk properties. *Astron. J.*
- Pöschel, T., and Schwager, T. 2005. *Computational Granular Dynamics*.
- Rein, H., and Latter, H. N. 2013. Large-scale N-body simulations of the viscous overstability in Saturn's rings. *Mon. Not. R. Astron. Soc.*
- Richardson, D. C. 1993. A new tree code method for simulation of planetesimal dynamics. *mnras*.
- Richardson, D.C. 1994. Tree code simulations of planetary rings. *Mon. Not. R. Astron. Soc.*, **269**, 493–511.
- Safranov, V. 1969. *Evolution of the protoplanetary cloud and the formation of the earth and planets*.
- Salo, H. 1987a. Collisional evolution of rotating, non-identical particles. *Moon Planets*, **38**, 149–181.
- Salo, H. 1987b. Numerical simulations of collisions between rotating particles. *Icarus*, **70**, 37–51.
- Salo, H. 1991. Numerical simulations of dense collisional systems. *Icarus*.
- Salo, H. 1992a. Gravitational wakes in Saturn's rings. *Nature*, **359**, 619–621.
- Salo, H. 1992b. Numerical simulations of dense collisional systems. II. Extended distribution of particle sizes. *Icarus*, **96**, 85–106.
- Salo, H. 1995. Simulations of dense planetary rings. III. Self-gravitating identical particles. *Icarus*, **117**, 287–312.
- Salo, H. 2001. Numerical Simulations of the Collisional Dynamics of Planetary Rings. Pages 330–349 of: Pöschel, T., and Luding, S. (eds), *Granular Gases*. Lecture Notes in Physics, Berlin Springer Verlag, vol. 564.
- Salo, H., and Karjalainen, R. 2003. Photometric modeling of Saturn's rings. I. Monte Carlo method and the effect of nonzero volume filling factor. *Icarus*, **164**, 428–460.
- Salo, H., and Schmidt, J. 2010. N-body simulations of viscous instability of planetary rings. *Icarus*, **206**, 390–409.
- Salo, H., Schmidt, J., and Spahn, F. 2001. Viscous overstability in Saturn's B ring: I. Direct simulations and measurement of transport coefficients. *Icarus*, **153**, 295–315.
- Salo, H., Karjalainen, R., and French, R. G. 2004. Photometric modeling of Saturn's rings. II. Azimuthal asymmetry in reflected and transmitted light. *Icarus*.
- Schmidt, J., and Salo, H. 2003. A weakly nonlinear model for viscous overstability in Saturn's dense rings. *Physical Review Letters*, **90**(6), 061102.
- Schmidt, J., Salo, H., Spahn, F., and Petzschmann, Olaf. 2001. Viscous overstability in Saturn's B ring: II. Hydrodynamic theory and comparison to simulations. *Icarus*, **153**, 316–331.
- Schmit, U., and Tscharnuter, W.M. 1995. A fluid dynamical treatment of the common action of self-gravitation, collisions, and rotation in Saturn's B-ring. *Icarus*, **115**, 304–319.
- Shu, F. H., and Stewart, G. R. 1985. The collisional dynamics of particulate disks. *Icarus*.
- Spahn, F., Hertzsch, J.-M., and Brilliantov, N.V. 1995. The role of particle collisions for the dynamics in planetary rings. *Chaos, Solitons and Fractals*, **5**, 1945–1964.
- Stewart, G. R., Lin, D. N. C., and Bodenheimer, P. 1984. Collision-induced transport processes in planetary rings. Pages 447–512 of: Greenberg, R., and Brahic, A. (eds), *Planetary Rings*. Tucson Arizona: Univ. of Arizona Press.
- Supulver, K. D., Bridges, F. G., and Lin, D. N. C. 1995. The coefficient of restitution of ice particles in glancing collisions: Experimental results for unfrosted surfaces. *Icarus*, **113**, 188–199.
- Tanaka, H., Ohtsuki, K., and Daisaka, H. 2003. A new formulation of the viscosity in planetary rings. *Icarus*.
- Thomson, F. S., Marouf, E. A., Tyler, G. L., French, R. G., and Rappoport, N. J. 2007. Periodic microstructure in Saturn's rings A and B. *Gephys. Res. Lett.*
- Toomre, A. 1964. On the gravitational stability of a disk of stars. *Astrophys. J.*, **139**, 1217–1238.
- Toomre, A. 1981. What amplifies the spirals. Pages 111–136 of: Fall, S. M., and Lynden-Bell, D. (eds), *Structure and Evolution of Normal Galaxies*.
- Toomre, A., and Kalnajs, A. J. 1991. Spiral chaos in an orbiting patch. Pages 341–358 of: Sundelius, B. (ed), *Dynamics of Disc Galaxies*. Almquist-Wiksell, Göteborg.
- Trulsen, J. 1972. Numerical simulation of jetstreams. I: The three-dimensional case. *Astrophys. Space Sci.*, **17**, 241–262.
- Ward, W. R. 1981. On the radial structure of Saturn's rings. *Gephys. Res. Lett.*, **8**, 641–643.
- Wisdom, J., and Tremaine, S. 1988. Local simulations of planetary rings. *Astron. J.*, **95**, 925–940.